이학박사 학위논문

Intraseasonal evolution characteristics of stratosphere-troposphere coupling in association with Arctic sea ice changes and Northern Hemisphere tropopause variability

북극 해빙 변화 및 북반구 대류권계면 변동성과 관련된 성층권-대류권 커플링의 계절내 진화 특성

2021년 8월

서울대학교 대학원

지구환경과학부

김 진 주

Intraseasonal evolution characteristics of stratosphere-troposphere coupling in association with Arctic sea ice changes and Northern Hemisphere tropopause variability

북극 해빙 변화 및 북반구 대류권계면 변동성과 관련된 성층권-대류권 커플링의 계절내 진화 특성

지도 교수 **Kwang-Yul Kim**

이 논문을 이학박사 학위논문으로 제출함

2021년 4월

서울대학교 대학원
지구환경과학부
김 진 주

김진주의 이학박사 학위논문을 인준함

2021년 6월

위 원 장	**최 우 갑**
부위원장	**김 광 열**
위 원	**김 정 훈**
위 원	**김 성 중**
위 원	**김 백 민**

Abstract

Variations in stratospheric polar vortex and associated stratosphere-troposphere interaction during boreal winter play an important role in the subseasonal prediction of tropospheric weather. In order to better understand stratosphere-troposphere interaction, this study scrutinizes intraseasonal evolutionary characteristics of stratospheric polar vortex fluctuations in terms of two different physical variables: sea ice and tropopause.

The leading two modes of winter Arctic sea ice cover variability and their linkage to stratospheric polar vortex variations are analyzed. The first mode represents an accelerating trend of Arctic sea ice decline associated with Arctic amplification, particularly in the Barents and Kara Seas. The second mode is associated with decadal-scale phase shifts of dipole sea ice anomalies in the North Atlantic caused by NAO circulation. The first two modes of sea ice variability represent respectively a forced climate change and internal variability. Sea ice reduction in the Barents and Kara Seas for the first mode is linked to a stratospheric vortex weakening during mid January–late February. The second mode with the dipole structure of positive sea ice anomalies in the Barents and Greenland Seas and negative anomalies in the Hudson Bay and Labrador Sea is related to a stratospheric vortex weakening during December–early February. The spatial evolutionary structure of anomalous polar vortex also exhibits differences between the two modes. When stratospheric anomalies are fully developed, stratospheric vortex is shifted to Eurasia in the first mode and to Europe in the second mode. These

two sea ice modes with different low-frequency variations partly contribute to a long-term mean change in subseasonal evolution of stratospheric polar vortex.

To identify general evolutionary characteristics in stratosphere-troposphere coupling, the leading modes of Northern Hemisphere tropopause variability for November–April and the associated stratosphere-troposphere variability were analyzed. The first two modes feature the intraseasonal evolution of tropopause pressure anomalies over the Arctic, which respond directly to stratospheric temperature fluctuations in association with stratospheric polar vortex variations. These two modes reflect the link between stratospheric polar vortex strength and high-latitude tropospheric circulation. The first mode represents a single-phase fluctuation of the stratospheric polar vortex from winter to early spring. The second mode describes a two-phase fluctuation of the stratospheric vortex with opposite signs in winter and in spring. Tropopause pressure anomalies near the mid-latitude tropospheric jet regions exhibit significant zonal variation. In the first mode, in particular, these mid-latitude tropopause anomalies are linked to asymmetric jet variations in the Atlantic and the Pacific regions. In regard to the Northern Annular mode, distinct vertical evolution structures of the two modes are practically related to the interannually varying structure of extreme vortex events with relatively long persistence. The results can help to improve the seasonal predictability of the Arctic climate by better understanding the evolutionary structure and potential timing of individual vortex events.

Keywords: stratosphere-troposphere coupling, Arctic sea ice variability, sea ice-stratospheric polar vortex relationship, tropopause variability, tropopause-stratospheric vortex relationship

Student Number: 2015-30983

List of publications

This thesis is based on the following research papers:

Chapter 3

Kim J, Kim K-Y (2020) Characteristics of stratospheric polar vortex fluctuations associated with sea ice variability in the Arctic winter. Climate Dynamics, 54:3599-3611.

Chapter 4

Kim J, Kim K-Y (2021) The leading modes of NH extratropical tropopause variability and their connection with stratosphere-troposphere variability. Climate Dynamics, 56:2413-2430.

Table of contents

List of figures

Chapter 1. Introduction

1.1. Background and motivation

During polar nights, the Northern Hemisphere stratosphere is dominated by the stratospheric polar vortex, which is characterized by very low temperature and cyclonic circulation. Variations in stratospheric polar vortex can affect not only the stratosphere but also the troposphere in a persistent manner (Baldwin et al. 2021). A downward coupling of the stratosphere with the troposphere is generally characterized by changes in stratospheric polar vortex strength, latitude of mid-latitude tropospheric jet and meridional gradient of surface pressure (Kidston et al. 2015). It also appears as a consistent evolutionary form of Northern Annular Mode (NAM) index with the same sign in the stratosphere and troposphere (Baldwin and Dunkerton 2001). Therefore, a better understanding of stratospheric vortex and stratosphere-troposphere coupled variability can be important in improving tropospheric weather predictions.

In recent decades, Arctic sea ice cover (SIC) has rapidly declined in association with the amplification of Arctic warming during winter (Cohen et al. 2014; Screen and Simmonds 2010; Serreze et al. 2009). Several studies suggest that Arctic SIC reduction tends to weaken stratospheric polar vortex through an enhancement of upward propagating planetary waves (Hoshi et al. 2017; Jaiser et al. 2016; Kim et al. 2014; Nakamura et al. 2015, 2016; Screen 2017a, 2017b; Yang et al. 2016; Zhang et al. 2018). This SIC-related stratospheric change affects tropospheric circulation in the form of negative

North Atlantic Oscillation (NAO)/Arctic Oscillation (AO).

In addition to the Arctic SIC loss associated with Arctic warming, Arctic SIC variations include contributions from natural variability such as AO/NAO. AO/NAO, considered as an atmospheric response to a change in Arctic SIC, is itself a major factor in regulating SIC variation (Hu et al. 2002; Magnusdottir et al. 2004; Serreze et al. 2007; Strong and Magnusdottir 2011). Deser et al. (2000) found from 1958–1997 data that the leading mode of winter Arctic SIC variability, characterized by an east-west dipole structure in the North Atlantic and weak dipole anomalies in the Pacific, is related to the AO/NAO. However, Yang and Yuan (2014) argued that the leading pattern of SIC variability has changed since 1998 as evinced in the rapid SIC reduction in the Barents-Kara Seas. The observed patterns of Arctic SIC during 1979–2007 reflected an upward trend of atmospheric circulation such as NAM until 1993. Since then, an overall decline of Arctic SIC is clearly observed despite the downward trend of NAM (Deser and Teng 2008). A multi-century model study by Strong and Magnusdottir (2010) suggests that the leading mode of SIC variation in the Atlantic sector of the Arctic Sea may change from an NAO-related dipole pattern to a n overall reduction pattern if the forced trend of SIC loss continues. In these studies, the two types of variations, corresponding to the overall loss of Arctic SIC and the dipole-like variation of Atlantic SIC, are found to play an important role in the total variability of winter Arctic SIC.

Previous studies have focused on the stratospheric vortex variation due to total SIC variability without distinguishing these two processes of SIC variability. Although several studies discussed distinct natures of atmospheric

responses to Arctic amplification and NAO/AO (Cohen et al. 2018; Hassanzadeh and Kuang 2015; Kim and Son 2016; Mori et al. 2014; Screen 2017b), it is not yet clearly understood how stratospheric circulation differs between these two distinct surface conditions. If we distinguish the continuing sea-ice reduction in the Barents-Kara Seas as a forced climate change and the dipole sea-ice variation as a natural variability, clearer picture of stratospheric variability under different sea ice conditions can be achieved.

Previous studies have paid much attention to changes in stratospheric vortex strength in association with Arctic SIC variability in the context of zonal mean (Cohen et al. 2014; McKenna et al. 2018) or annular mode (Jaiser et al. 2016; Kim et al. 2014; Screen 2017a; 2017b; Zhang et al. 2018). The geometric features of stratospheric vortex are also an integral part of understanding polar vortex variability (Lawrence and Manney 2018; Mitchell et al. 2011; Seviour et al. 2013). In this respect, Zhang et al. (2016) showed that stratospheric vortex continued to move toward Eurasia as Arctic SIC decreases. The spatio-temporal evolution of stratospheric disturbances, however, may change according to the SIC modes, and lead to distinct structural patterns of stratospheric vortex.

In addition to investigating stratospheric variability due to certain tropospheric sources, there have been many efforts to understand the general characteristics of stratosphere-troposphere coupling (Baldwin and Dunkerton 2001; Limpasuvan et al. 2004; 2005). Previous studies mainly dealt with composite mean characteristics of vertical evolution during stratospheric extreme vortex events. An extreme event is determined by the amplitude of a

stratospheric vortex defined in perspective of its zonal mean or as an annular mode. In case of a vortex weakening event, it is further classified into a displacement or a split type based on the vortex shape (Charlton and Polvani 2007). However, these approaches do not fully account for the spatio-temporal evolution of a stratospheric vortex that may affect the coupling structure. Regionally distinct changes in a stratospheric vortex may produce zonally asymmetric features in the tropopause and the troposphere (Mitchell et al. 2013; Seviour et al. 2016; Thompson and Wallace 2000). Tropospheric jet responses in relation to stratospheric vortex fluctuations, for example, are often stronger in the Atlantic sector than in the Pacific sector, and this pattern is closer to the North Atlantic Oscillation (NAO) pattern than the Arctic Oscillation (AO) (Davini et al. 2014; Hitchcock and Simpson 2014). In this regard, viewing stratospheric variation in a zonal symmetry sense may not be sufficient to understand these zonally asymmetric characteristics of stratosphere-troposphere coupling. In order to understand the connectivity of the stratosphere and the troposphere in detail, therefore, it is necessary to investigate both the spatial and the temporal evolution patterns of vertical coupling.

However, not all stratospheric vortex fluctuations lead apparent tropospheric variation (Jucker 2016; Runde et al. 2016; White et al. 2018). Mitchell et al. (2013) describe that the tropospheric response to stratospheric vortex variation depends on the type of sudden stratospheric warming, such as vortex displacement or vortex split. Some studies argue that the depth of initial stratospheric disturbance (Gerber et al. 2009; Hitchcock et al. 2013)

and the strength and persistence of the variation in the lower stratosphere (Hitchcock and Simpson 2014; Maycock and Hitchcock 2015; Runde et al. 2016) or the tropopause region (Jucker 2016) are important in determining the tropospheric response to stratospheric vortex variation. Strong and persistent vortex variation at the lower stratosphere can affect the troposphere through tropospheric eddy flux (Kidston et al. 2015; Limpasuvan and Hartmann 2000; Simpson et al. 2009), and through the anomalous tropospheric relative vorticity induced by the tropopause height fluctuation (Ambaum and Hoskins 2002; Lorenz and Deweaver 2007; Tomassini et al. 2012). In this context, tropopause can be an important factor in understanding stratospheric vortex fluctuations and their coupling with tropospheric fluctuations.

1.2. Objectives

The purpose of the first part (chapter 3) is to extract Arctic sea ice reduction signal and North Atlantic sea ice dipole signal and to understand their linkage with distinct stratospheric polar vortex variations. The stratospheric polar vortex variations for two different sea ice modes are analyzed not only in terms of intensity but also in terms of horizontal and vertical structures.

The purpose of the second part (chapter 4) is to identify the leading modes of extratropical tropopause fluctuations in the Northern Hemisphere winter season. Focusing on the spatio-temporal evolution patterns, it is investigated how tropopause anomalies evolve in association with stratospheric and tropospheric anomalies. On top of the zonal mean structures, characteristics of regional variability are also discussed particularly in the Atlantic and Pacific jet regions. Furthermore, it is examined how the vertical evolution associated with the leading modes of tropopause fluctuations are related to year-to-year variability of stratospheric vortex events.

Chapter 2. Data and Methodology

2.1. Data

Data used in chapter 3 derive from the 1979-2018 ERA interim daily reanalysis product (Dee et al. 2011) at 1.5°×1.5° resolution for the Northern Hemisphere (> 30°N). Each winter consists of 120 days from November 1 to February 28; leap days are removed. This period is particularly chosen in order to isolate the winter anomaly patterns of SIC without much contamination from the widespread pattern of SIC reduction in fall (Kim et al.2016). Major modes of Arctic SIC variability are extracted from sea ice area fraction (concentration) data north of 40.5°N. The SIC analysis in the present study is robust as also confirmed by another sea ice concentration data from National Snow and Ice Data Center (NSIDC at nsidc.org). 37 pressure-level (1000–1 hPa) variables and potential vorticity on 6 potential temperature surfaces (430, 475, 530, 600, 700, and 850 K) are analyzed.

Major modes of tropopause variability in chapter 4 are extracted from 5-day mean tropopause pressure data of 40-year (1979–2019) NCEP daily reanalysis product at 2.5°×2.5° resolution for the Northern Hemisphere (30°–87.5°N). The tropopause definition used in this study is based on lapse-rate criterion (WMO, 1957). Each year represents the 36 pentad-mean data from November 1 through April 29; leap days are removed. Pressure at 2PVU level from ERA interim data is also used to validate the leading modes from NCEP tropopause pressure. 5-day mean ERA interim daily data at 37 pressure levels (1000–1 hPa) are analyzed for the same period (1979–2018).

2.2. Methodology

In order to extract accurate physical mechanisms from the variables above, the cyclostationary empirical orthogonal function (CSEOF) technique is used (Kim 2017; Kim et al. 1996; Kim and North 1997; Seo and Kim 2003). Data, $T(r,t)$, are decomposed into mutually orthogonal CSEOF loading vectors (CSLV) and mutually uncorrelated principal component (PC) time series:

$$T(r,t) = \sum_n CSLV_n(r,t)\, PC_n(t),$$

$$CSLV_n(r,t) = CSLV_n(r,t+d),$$

where r and t denote space and time, and d is the nested period of CSEOF analysis. Each CSLV consists of spatiotemporally varying patterns within the nested period, which describes a distinct physical process of each mode. In chapter 3, the nested period is set to 120 days (from November 1 to February 28), and in chapter 4, it is set to 36 pentads (from November 1 to April 29). The magnitude of CSLV varies according to corresponding PC (amplitude) time series.

Regression analysis in CSEOF space (Kim et al. 2015) is conducted to identify key variable's evolution process that is physically consistent with each of the leading modes of target variable. First, CSEOF analysis is performed individually on several key variables. Then, regression analysis in CSEOF space is carried out in the following manner:

$$\text{Step 1: } PC_n^{(\text{target})}(t) = \sum_{m=1}^{M} \alpha_m^{(n)} PC_m^{(\text{predictor})}(t) + \varepsilon^{(n)}(t),$$

$$\text{Step 2: } CSLV_n^{(\text{reg})}(r,t) = \sum_{m=1}^{M} \alpha_m^{(n)} CSLV_m^{(\text{predictor})}(r,t),$$

where $PC_n^{(\text{target})}(t)$ is the nth PC time series of the target variable (sea ice area fraction in chapter 3 and tropopause pressure in chapter 4), $CSLV_m^{(\text{predictor})}(r,t)$ and $PC_m^{(\text{predictor})}(t)$ are the mth CSLV and PC time series of another variable (called the predictor variable), $\alpha_m^{(n)}$ and $\varepsilon^{(n)}(t)$ are regression coefficient and regression error time series, respectively. The regressed CSLV of the predictor variable, $CSLV_n^{(\text{reg})}(r,t)$, evolves in consistence with the nth mode of target's variability. After regression analysis in CSEOF space, the entire dataset can be written in the form:

$$Data(r,t) = \sum_n \{\mathrm{T}_n(r,t), \mathrm{Z}_n(r,t), \mathrm{U}_n(r,t), \cdots\} PC_n^{(\text{target})}(t),$$

where the terms in curly braces are (regressed) loading vectors derived from different variables. They share the PC time series of target's variability and are regarded as physically consistent with each other. Patterns in all nested periods of CSLV are examined but for the sake brevity time-mean or area-mean evolutions are used to highlight notable features. The results are based on anomalies after the seasonal cycle is removed.

Chapter 3. Characteristics of stratospheric polar vortex fluctuations associated with sea ice variability in the Arctic winter

3.1. Leading modes of Arctic sea ice variability in winter

Figure 3.1 shows monthly averaged patterns of the first two leading modes of daily SIC anomalies during November–February. SIC anomalies develop within the seasonal excursion of SIC boundaries (magenta and navy contours in Figs. 3.1a–d and 3.1f–i). Similar SIC patterns can be obtained by conducting EOF analysis followed by composite analysis.

The first CSEOF mode represents Arctic SIC reduction throughout the winter and accounts for ~29% of the total variance; SIC reduction is particularly prominent in the Barents and Kara Seas (BKS). The corresponding PC time series shows an accelerating trend of Arctic SIC decline together with naturally occurring interannual variability; the rate of SIC reduction appears to have increased significantly since 2004/2005 (Fig. 3.1e).

The second CSEOF mode exhibits a dipole pattern from December with anomalies of opposite signs between the east and west of the North Atlantic. Weak SIC anomalies are also seen in the Pacific sector. This mode explains ~9% of the total variance. It is known that this dipole pattern of SIC change is associated with North Atlantic Oscillation (NAO) (Deser et al. 2000; Strong and Magnusdottir 2010). The PC time series of the second mode shows interannual and decadal-scale fluctuations of SIC dipole anomalies (Fig. 3.1j)

and is correlated at –0.4 with a ±60-day smoothed NAO index. From the mid-1990s to the early-2010s, positive SIC anomalies in the eastern North Atlantic (Barents and Greenland Seas) and negative anomalies in the western North Atlantic (Hudson Bay and Labrador Sea) have been frequently observed (Fig. 3.1j). In recent few years, the amplitude of the dipole pattern has been small. The low-frequency variation of the second mode is similar to that of Atlantic Multidecadal Oscillation (figure not shown). This means that oceanic process may play an important role in the decadal phase shift of the dipole SIC anomalies in the North Atlantic.

Arctic warming is conspicuous in the first mode (Fig. 3.2a–d). Atmospheric warming coexists with sea ice decline in the BKS and Chukchi Sea (Figs. 3.1a–d and 3.2a–d), which is significantly related to increased heat flux over the region of sea ice reduction (Kim et al. 2016, 2019; Screen and Simmonds 2010). Warm SST anomalies are also seen near the region of sea ice loss (figure not shown). The positive air temperature anomaly in the Pacific sector of the Arctic Ocean is seen for November–December, but the positive anomaly in the BKS persists throughout the winter (Figs. 3.2a–d). Weak cooling over Siberia and East Asia can be explained via cold advection due to the anticyclone centered in the BKS (Kim and Son 2016; Zhang et al. 2018). Warm Arctic and cold Eurasia is a characteristic pattern of Arctic amplification associated with Arctic SIC decline (Cohen et al. 2014; Mori et al. 2014; Overland et al. 2011). The positive height anomaly around the region of BKS warming, which becomes stronger in January, is a prominent feature of mid-tropospheric circulation in the first mode. In addition, negative height

anomaly over Siberia and East Asia seems to be associated with Rossby wave response to SIC reduction in the BKS (Honda et al. 2009; Kim et al. 2014; Nakamura et al. 2015).

A weakening of the meridional temperature gradient and westerly wind associated with BKS warming is also advantageous for an increase in regional blocking occurrences (Cohen et al. 2020; Luo et al. 2016). The anomalous anticyclone around the BKS may be associated with more frequent and persistent Ural blocking. However, causality between tropospheric circulation, such as anticyclone around the BKS (Ural blocking) or Eurasian cooling, and SIC reduction in the BKS is still questionable. Some studies suggest that tropospheric variation is caused by the SIC reduction in BKS (Kim et al. 2014; McKenna et al. 2018; Mori et al. 2014; Zhang et al. 2018), while others suggest that tropospheric variation represents internal climate variability (Blackport et al. 2019; Peings 2019 and references therein).

The second mode shows positive mid-tropospheric geopotential height anomalies around the Iceland and southern Greenland and negative anomalies along ~40°N of the North Atlantic (Fig. 3.2e–h). This structure is salient in December–January and resembles the negative phase of NAO. The accompanying temperature anomalies in high latitudes display opposite variations between the eastern and western hemispheres. In November, warm anomalies develop around the Hudson-Baffin Bay and the Chukchi Sea where negative SIC anomalies exist (Fig. 3.2e). Anomalous anticyclone established over the Greenland from late November advects cold (warm) air toward the Barents Sea and northern Europe (the Labrador Sea and the Baffin Bay).

Accordingly, cold anomalies will increase SIC over the Barents and the Greenland Seas and warm anomalies will reinforce SIC decline over the Hudson Bay and the Labrador Sea (Fig. 3.2f). This anomalous anticyclone can also be considered as a regional blocking enhancement. In fact, the SIC decline in the west of Greenland and the negative NAO are related to the increase in Greenland blocking duration (Chen and Luo 2017).

The circulation change is physically consistent with the dipole pattern of SIC anomaly, which is seen from late November (Figs. 3.1f–i). Warm SST anomaly in the Labrador Sea and cold SST anomaly in the Barents-Greenland Seas coincide with the opposite signs of SIC anomalies (figure not shown). Existing SST anomalies seem to be intensified with the development of NAO-like circulation and reach its maximum in January. Therefore, the second mode can be interpreted as a dipole SIC variation in the Atlantic sector driven by NAO-like atmospheric circulation (Deser et al. 2000; Deser and Teng 2008).

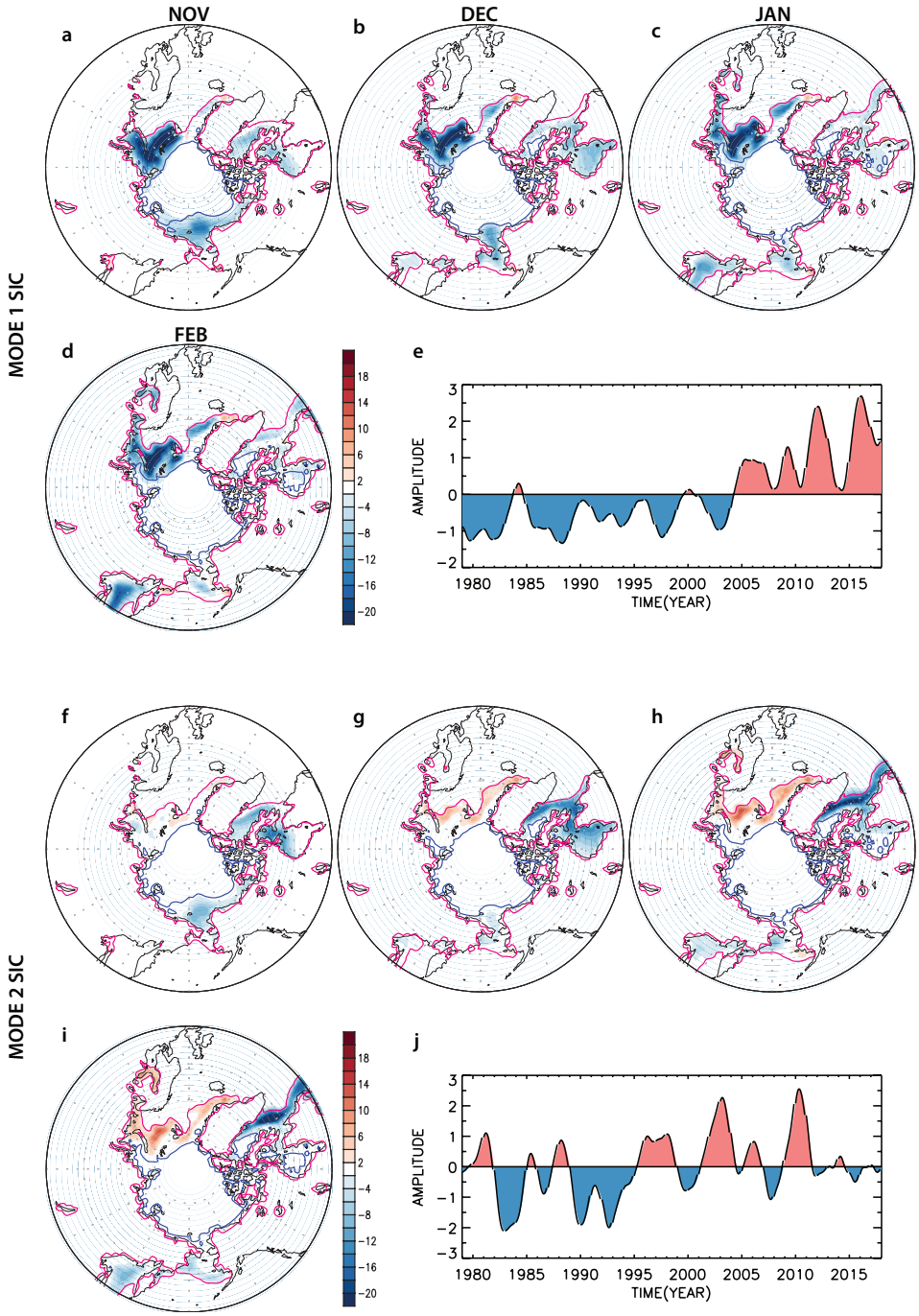

Figure 3.1. Monthly-averaged patterns of anomalous sea ice cover (%) for (a–d) the first and (f–i) the second CSEOF mode derived from the November–February sea ice area fraction (concentration) data over the domain (40.5°–87°N), and (e and j) the corresponding PC time series. The magenta and navy contours represent 5% and 95% sea ice isopleths in the climatological seasonal cycle.

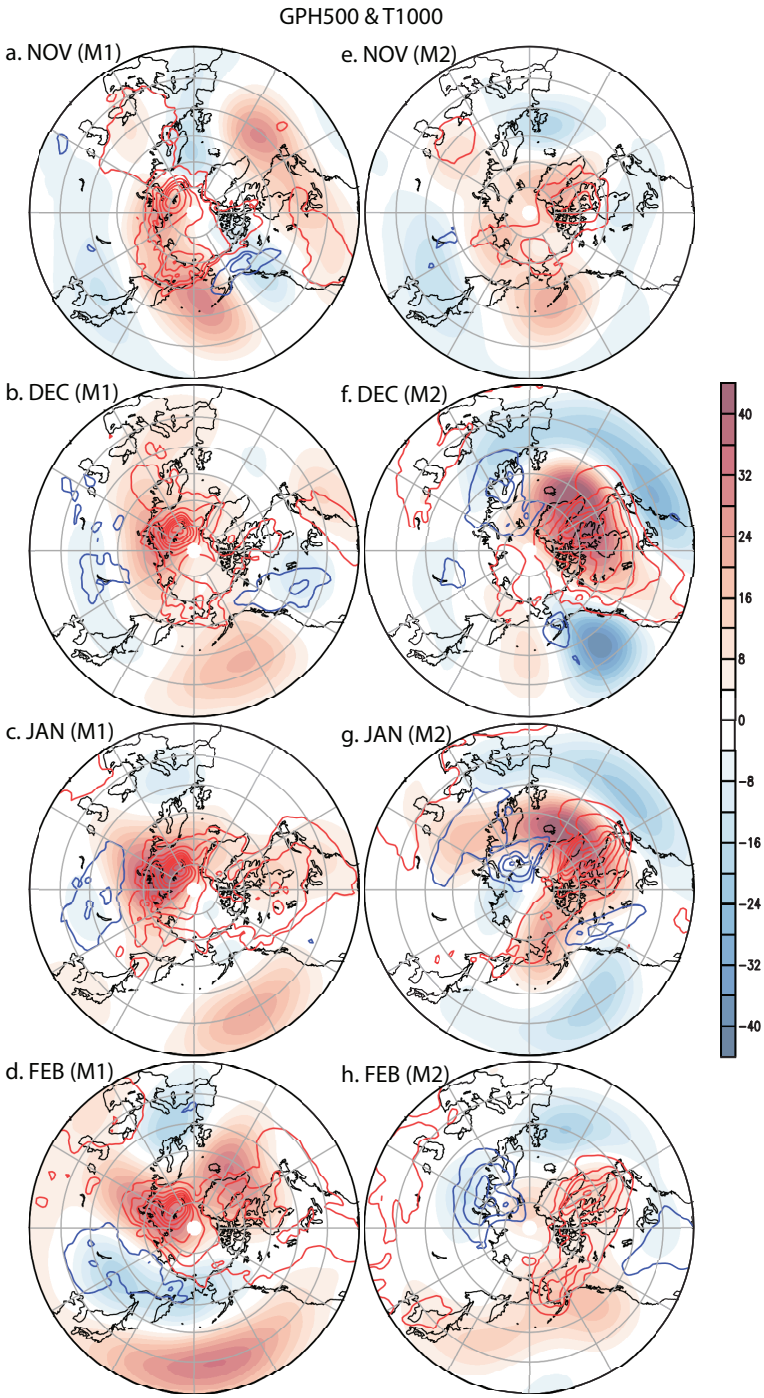

Figure 3.2. Monthly-averaged patterns of 500-hPa geopotential height anomalies (shading) and 1000-hPa air temperature anomalies (red (+) and blue (–) contours at 0.5K interval) for (a–d) the first CSEOF mode and (e–h) the second mode of sea ice variability.

3.2. Variation of stratospheric polar vortex strength

Figure 3.3 displays vertical evolutions of polar-cap [0°–360°E, 64.5°–87°N] mean geopotential height (PCH), temperature (PCT), and zonal-mean zonal wind anomalies. They, as a proxy for the Northern annular mode (Baldwin and Dunkerton 2001; Baldwin and Thompson 2009), describe variations in strength of stratospheric polar vortex. The positive anomalies in the stratospheric PCH indicate a weakening of stratospheric polar vortex. The two leading modes of SIC variability show different evolution of PCH (Fig. 3.3a and 3.3b). In the first mode, positive PCH anomaly develops strongly in the stratosphere from mid-January following the negative anomaly in December, and eventually extends to the troposphere. The positive PCH coincides with a deceleration of the polar night jet and an increase in Arctic stratospheric temperature (Fig. 3.3a and c). This pattern indicates that a strong winter reduction of Arctic SIC is linked with stratospheric vortex weakening during mid-January–late February. In late February, there is still positive PCH anomaly in the stratosphere but it is weak and develops at relatively low altitudes.

The second mode, which corresponds to positive SIC anomaly in the Barents and Greenland Seas and negative anomaly in the Labrador Sea and Hudson Bay (Fig. 3.1f–i), shows positive PCH and PCT anomalies in the stratosphere from December to early February together with anomalous easterly wind (Fig. 3.3b and d). The positive anomalies persist through February in the lower stratosphere. Anomalous stratospheric vortex

strengthening comes after the vortex weakening. Unlike the first mode, the negative PCT anomalies occurring after the vortex weakening are stronger than that before the vortex weakening in November. The vortex strengthening, however, is limited to the stratosphere.

Figure 3.3e and 3.3f show the evolution of vertical Eliassen-Palm (EP) flux at 100 hPa and divergence of EP flux at 10 hPa. The total convergence of EP flux anomalies in the leading SIC modes is dominated by the vertical component of EP flux anomalies, associated mainly with upward propagations of EP flux (figure not shown). In the first mode, upward EP flux anomalies are dominant near 60°N from early January, just before upper-stratospheric anomalous easterly develops, to the end of January, just before upper-stratospheric anomalous easterly reaches its maximum (Fig. 3.3e). The anomalous upward EP flux converges at higher altitudes, resulting in the deceleration of stratospheric westerly wind and the weakening of stratospheric polar vortex (Figs. 3.3a and e). In the second mode, upward EP flux anomaly and its convergence during December–January are dynamically consistent with occurrence of upper-stratospheric anomalous easterlies and explain each extremum of easterly wind reasonably (Fig. 3.3f). During mid–late January, anomalous convergence is limited to high latitudes and anomalous divergence begins to develop in lower latitudes.

Figure 3.4 shows temporal evolution of vertical EP flux anomalies at 100 hPa divided into linear and nonlinear components. The total vertical EP flux of both modes evolves in a similar manner to the linear component. However, the contribution of the nonlinear component to the total flux is not

significantly smaller than that of the linear component. In the first mode, during January when the westward forcing on stratospheric zonal wind is dominant (Figs. 3.3a and e), the linear part of upward EP flux anomaly is explained mainly by the zonal wavnumber-1 component except in mid-January, when the zonal wavenumber-2 component contributes greatly (Fig. 3.4a). In the second mode, the linear component dominates from late December to early January (Fig. 3.4b). Much of the linear component of vertical EP flux developing in December–January is associated with the WN1 component. The WN2 component induces a downward propagation during mid-December–early January, but its amplitude is much smaller than the WN1 component.

Upward EP flux anomalies can be partly explained in terms of linear constructive interference between climatological planetary-scale waves and SIC-related wave anomalies (Garfinkel et al. 2010; Nishii et al. 2009; Smith et al. 2010; Smith and Kushner 2012). Anomalous high around the BKS and anomalous low around Siberia in the first mode (Fig. 3.5a–f), and anomalous high around the Greenland in the second mode are advantageous for increasing upward propagation of EP flux through amplification of climatological waves (Fig. 3.5g–l). This relationship is consistent with other studies suggesting that increase in blocking frequencies around the Ural region and southern Greenland is associated with the enhancement of upward propagating planetary-scale waves (Martius et al. 2009; Peings 2019). The anomalous highs may reflect an increase in the frequency and duration of Ural blocking in the first mode and Greenland blocking in the second mode.

However, in addition to the linear interference, increase in upward propagation of EP flux is attributable to non-negligible nonlinear part associated with interactions among anomalous waves (Fig. 3.4).

The stratospheric vortex variation depends on how well the tropospheric circulation amplifies climatological waves and thus increases the upward propagation of the waves. Thus, although SIC reduction and the resulting warming over the BKS are already strong from November in the first mode, substantial wave propagation occurs only after mid–December. As a result, strong vortex weakening in the first mode appears later than in the second mode.

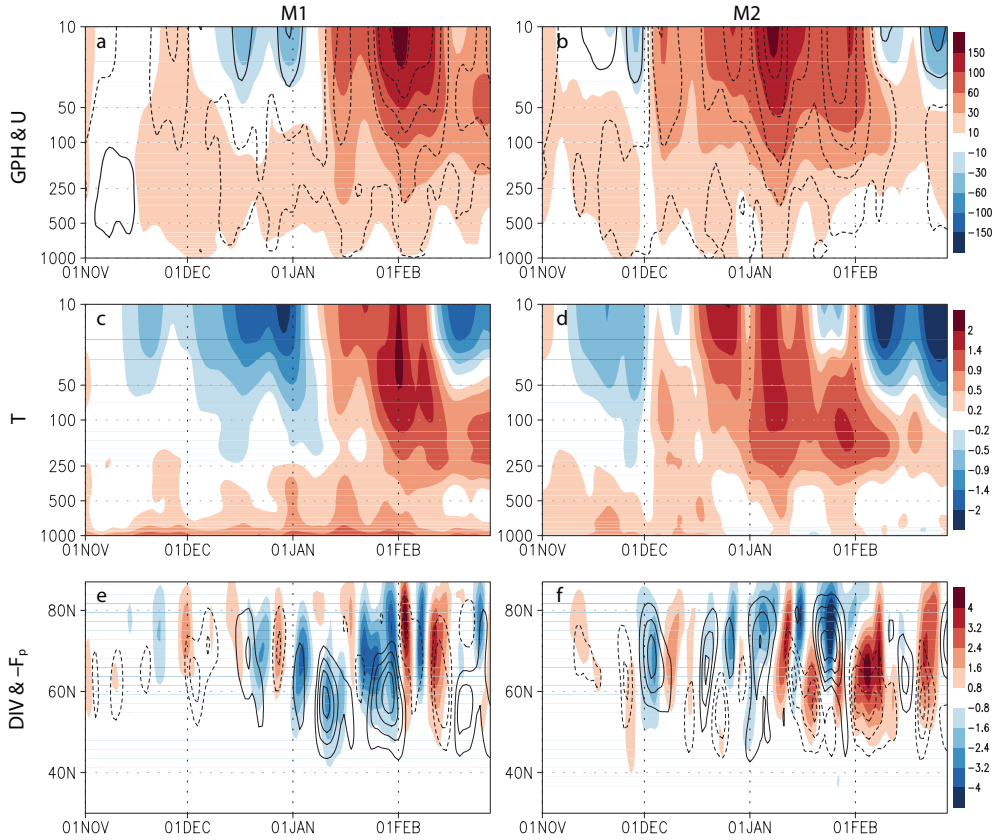

Figure 3.3. Time-altitude pattern of (a and b) polar cap [0°–360°E, 64.5°–87°N] mean geopotential height (shading) and zonal-mean zonal wind at 60°N (contoured at 1.0 m s^{-1} interval from ±0.5 m s^{-1}) and (c and d) polar cap mean air temperature anomalies, and (e and f) time-latitude evolution of the divergence of EP flux anomaly at 10 hPa (shading) and the vertical component of EP flux at 100 hPa (contoured at 1×10^5 Pa m^2 s^{-2} interval, positive upward) for the first (left column) and second (right column) CSEOF modes.

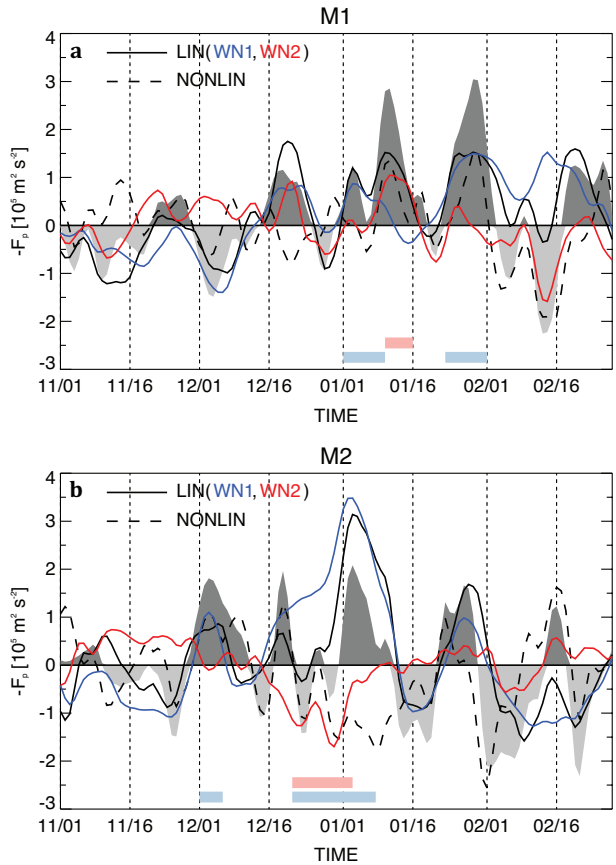

Figure 3.4. Vertical component of latitude-averaged [49.5°–79.5°N] EP flux at 100 hPa (positive upward) and contributions from the linear component (black solid) and nonlinear component (black dashed) of vertical EP flux in the (a) first and the (b) second CSEOF modes. The linear component is further decomposed into the zonal wavenumber-1 (blue) and zonal wavenumber-2 (red) components. The period represented by the blue (red) shaded bar is used for the composite analysis in Fig. 3.5 to identify any notable patterns of the anomalous geopotential height associated with the WN1 (WN2) components of the vertical EP flux during stratospheric vortex weakening.

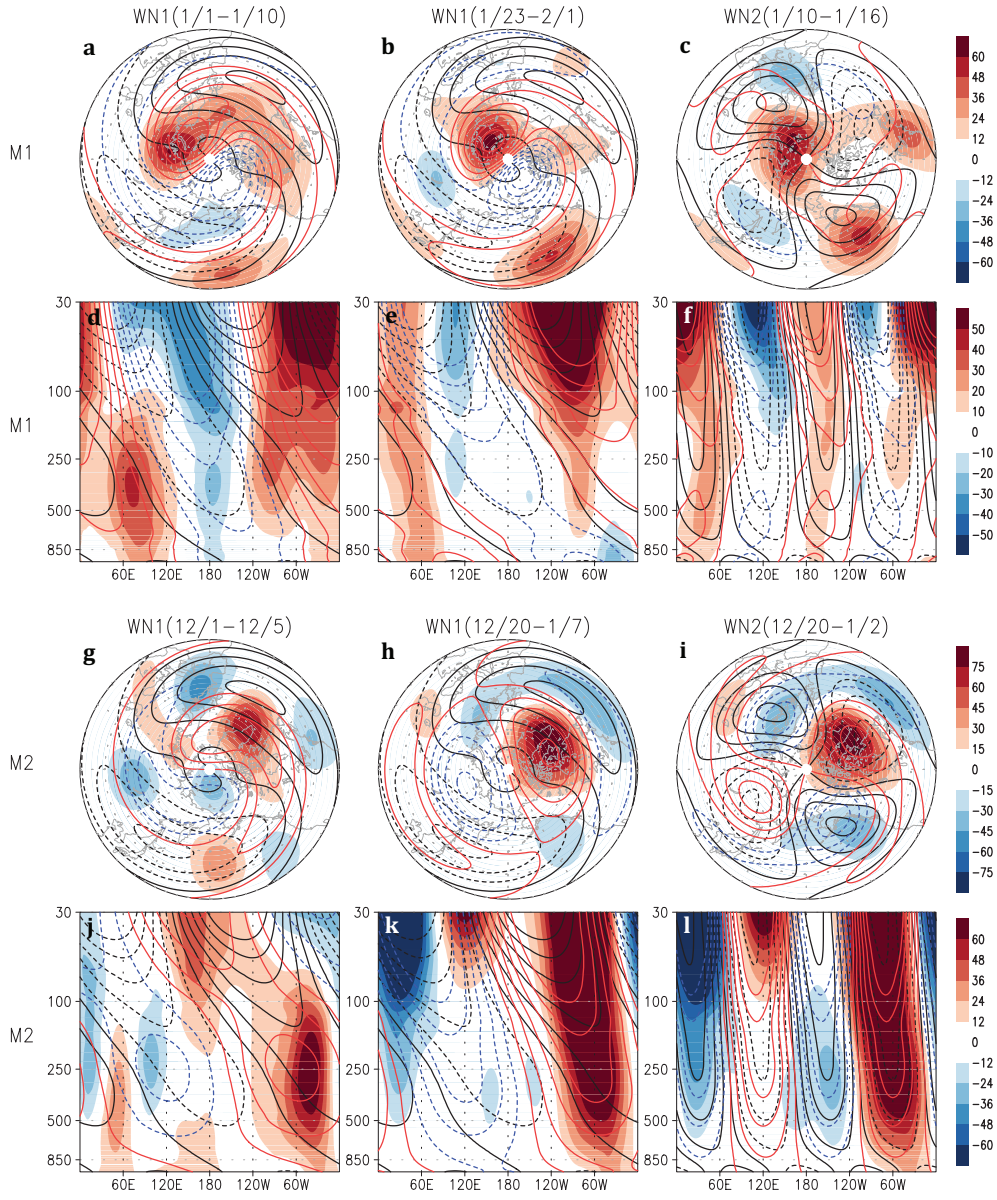

Figure 3.5. Time-averaged (a–c and g–i) 250-hPa horizontal pattern and (d–f and j–l) longitude-altitude pattern at 60°N of geopotential height anomalies (shading) in the (a–f) first and (g–l) second modes, and the zonal wavenumber-1 and the zonal wavenumber-2 components of climatological geopotential height (black contour) and geopotential height anomalies (red contour: zero and positive, blue contour: negative). Each pattern is averaged over the period shown in Fig. 3.4 (blue and red shaded bars).

3.3. Geometric characteristics of stratospheric anomalies during polar vortex weakening

Variation in the strength of stratospheric vortex is estimated in terms of zonal-mean and Arctic-mean anomalies (Fig. 3.3). It should be noted, however, that stratospheric anomalies are neither zonally symmetric nor their centers are at the pole. In this regard, area mean or zonal mean field is not a sufficiently accurate depiction of stratospheric vortex variations. To characterize the detailed evolution of stratospheric anomalies, therefore, geometric structures of anomalies should be examined further.

In this thesis, polar vortex edge in Figs. 3.6k–o and 3.7k–o, and 3.9c and 3.9f is represented by a constant value of potential vorticity (PV). Vortex edge is determined by the mean value of climatological PV at the maximum gradient at each longitude. This approach is similar to that in earlier studies (Lawrence and Manney 2017; Nash et al. 1996; Zhang et al. 2018). In Figs. 3.6k–o and 3.7k–o, vortex edge is determined to be 54 PVU from the vertically averaged (430–600 K) PV field. For Fig. 3.9c and 3.9f, PV value at the vortex edge is normalized at each isentropic surface. Then, normalized PV value of 1 is used to define the vortex edge. The vortex edge value at each isentropic surface is used as a scaling factor to display a three-dimensional structure of potential vorticity anomalies in similar orders of magnitude across the stratosphere.

Figures 3.6 and 3.7 show the five-stage horizontal evolution of stratospheric anomalies corresponding to the development of the polar vortex

weakening. Based on the date of the maximum intensity of 10-hPa PCH anomaly, the vortex weakening event is divided into five stages between Jan 5–Feb 28 (11-day interval) for the first mode, and Nov 26–Feb 18 (17-day interval) for the second mode. Since the duration of the anomalous positive stratospheric PCH in the first mode is shorter than in the second mode (Fig. 3.3), we used 11-day averaged patterns for the first mode and 17-day averaged pattern for the second mode.

For the first mode, positive height anomaly develops in the upper stratosphere from the subpolar region and covers the entire Arctic (> 65°N) by stage 3 when the anomalous positive PCH reaches its maximum (Figs. 3.6a–c). The mature phase of the positive height anomaly is circular and its center of action is slightly shifted toward North America (Fig. 3.6c). The positive anomaly is surrounded by negative anomalies and the anomalous easterly along the boundary of the positive height anomaly extends to lower latitudes (~30°N) in the western hemisphere (Fig. 3.6h). During stages 4 and 5, the negative height anomalies in mid-latitudes expand toward the pole and the positive anomaly over the polar region is attenuated in the form of an ellipse (Figs. 3.6d and e).

The positive temperature anomalies and the negative potential vorticity (PV) anomalies over the Arctic (Figs. 3.6f–o) are physically consistent with the positive height anomalies. The PV anomalies reflect the lower stratospheric variations and strong negative anomalies in the Arctic persist in later stages (Figs. 3.6m–o). In addition to the decreasing intensity of the stratospheric polar vortex, the edge of vortex based on a constant value of the

climatological potential vorticity shows a slight shift of vortex toward Eurasia in stage 3 (magenta contour line in Fig. 3.6m), a result similar to Zhang et al. (2016). This is because the strong negative PV anomaly over the northern Canada acts to move the western edge of the vortex toward the Pole and the weak positive anomaly in the subpolar Eurasia acts to move the eastern edge toward the south (Fig. 3.6m).

The position of maximum zonal wind speed, another definition of the boundary of stratospheric polar vortex (Waugh et al. 2016), also shows a similar shift in the upper stratosphere (10 hPa) (Fig. 3.8c). While in the lower stratosphere southward migration of the vortex boundary is seen uniformly in the Eurasia region, in the upper stratosphere it is more pronounced in Siberia and the North Atlantic (Figs. 3.6m and 3.8c). Thus, in the upper stratosphere, the extension of vortex to these directions (Siberia and the North Atlantic) is more noticeable than the movement toward Eurasia (Figs. 3.9c). In addition, polar night jet slows down except in 10°–60°E (Fig. 3.8c). This uneven change indicates that the pattern of zonal-wind anomalies during the vortex weakening does not necessarily coincide with that of climatological wind (Fig. 3.6m).

For the second mode, positive geopotential anomaly is developed from the northeastern Russia in stage 1 and occupies the polar region in stage 3 (Fig. 3.7a–c). In stage 3, the positive anomaly is elongated in the 90°E–90°W direction and has a bean-like shape that envelops the negative anomaly over Europe. The maximum height anomaly is shifted toward North America as in the first mode. Unlike the first mode with a low anomaly, however, the second

mode shows a high anomaly in Siberia (Figs. 3.6c and 3.7c). The anomalous easterly has an elongated spiral pattern along the high anomaly and extends to 30°N in the eastern hemisphere (Fig. 3.7h). The anomalous easterly contributes to slowing down polar night jet except in western Eurasia in which the anomalous westerly rather enhances local polar night jet (Fig. 3.8h). In stages 4 and 5, this positive height anomaly retreats toward Europe, and the negative anomaly over North America spreads toward the North Pole and becomes stronger (Figs. 3.7d and e).

Temperature and potential vorticity anomalies evolve in a similar fashion with the geopotential height anomalies (Figs. 3.7f–o). In stage 3, the positive PV anomaly over Europe and the negative PV anomaly over the northern Canada push the vortex to shift toward Europe (Figs. 3.7m and 3.9f). Polar night jet in the upper stratosphere (10 hPa) more clearly shows the vortex movement toward Europe (Fig. 3.8h). In phase 5, however, the negative PV anomaly moves toward Europe and weak positive anomaly appears over the northern Canada (Fig. 3.7o).

The stratospheric polar vortices of the two modes not only show distinct evolutions in terms of timing and duration as can be seen in the development of polar cap averaged or zonally averaged anomalies (Fig. 3.3), but also exhibit different spatio-temporal structures of evolution (Figs. 3.6–3.9). The zonally asymmetric distribution of the anomalies in the mature phase contributes to a stratospheric vortex migration toward Eurasia in the first mode and toward Europe in the second mode (Figs. 3.6m, 3.7m, 3.8c and 3.8h). According to three-dimensional pictures, although there are differences

in degree, the first mode shows the vortex shift toward Eurasia in all layers. However, the second mode exhibits a different structure in the vertical direction: the vortex shifts toward Europe in the upper layers but prominently toward east of Europe in the very lower layers (Fig. 3.9). The circulation patterns for the two modes also differ in the troposphere (Figs. 3.6a–e and 3.7a–e). Stratospheric vortex weakening is accompanied by strong anticyclone near the BKS in the first mode (Fig. 3.6a–c), and strong anticyclone in the southern Greenland in the second mode (Fig. 3.7a–c).

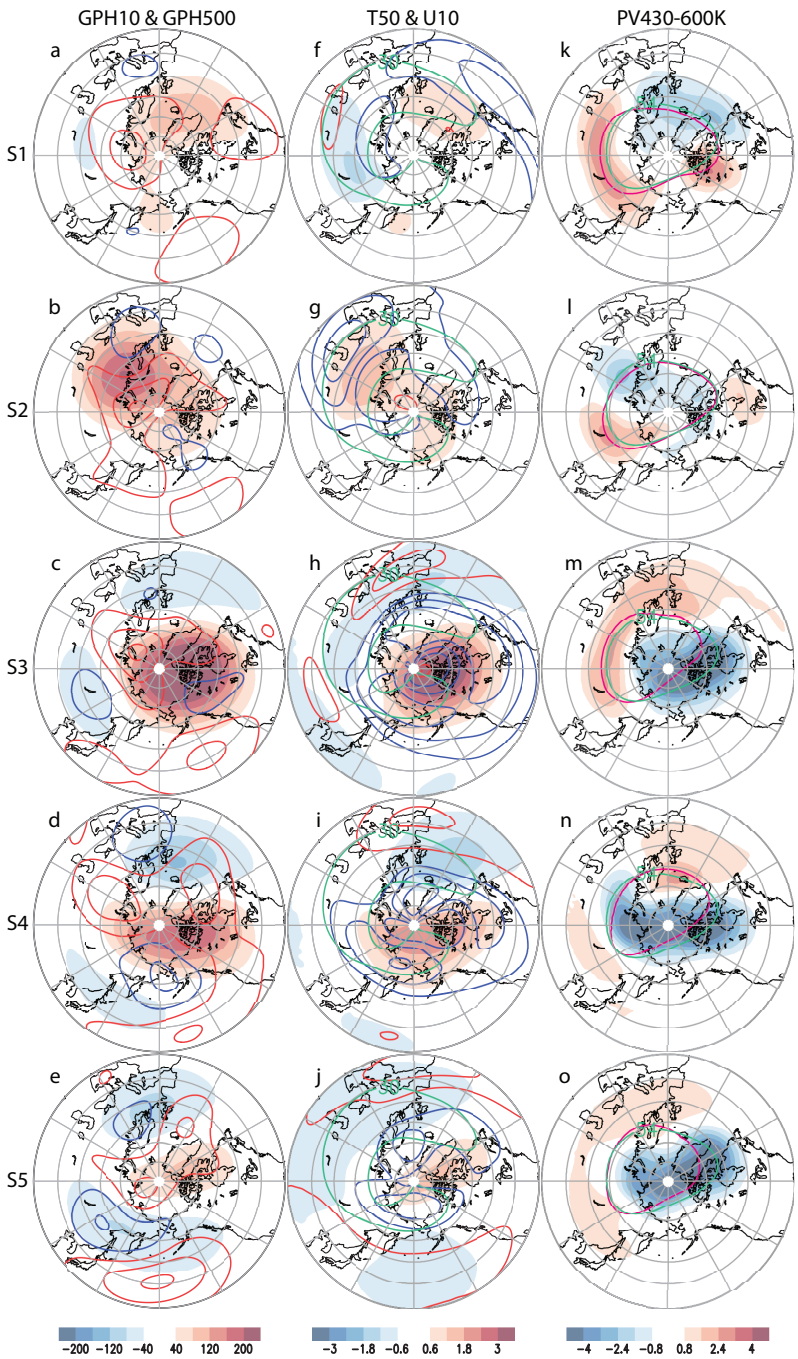

Figure 3.6. Five-stage evolution of (a–e) 10-hPa (shading) and 500-hPa (red (+) and blue (–) contours at ±10, 30, and 50 m) geopotential height anomalies, (f–j) 50-hPa temperature anomalies (shading) and 10-hPa zonal wind (red and blue contours at ±2, 4, and 6 m s^{-1}) with climatological 30 m s^{-1} zonal wind (aqua contour), and (k–o) the vertically averaged (430–600 K) potential vorticity anomalies (shading, 0.8 PVU (10^{-6} K m^2 kg^{-1} s^{-1}) interval) with climatological potential vorticity (aqua contour at 54 PVU) and the perturbed

potential vorticity (magenta contour at 54 PVU) for the first CSEOF mode. The perturbed potential vorticity is obtained by adding the climatology with the 2σ values of the anomalous potential vorticity. Each pattern represents an 11-day average based on the development of positive PCH anomaly at 10 hPa with its maximum in stage 3.

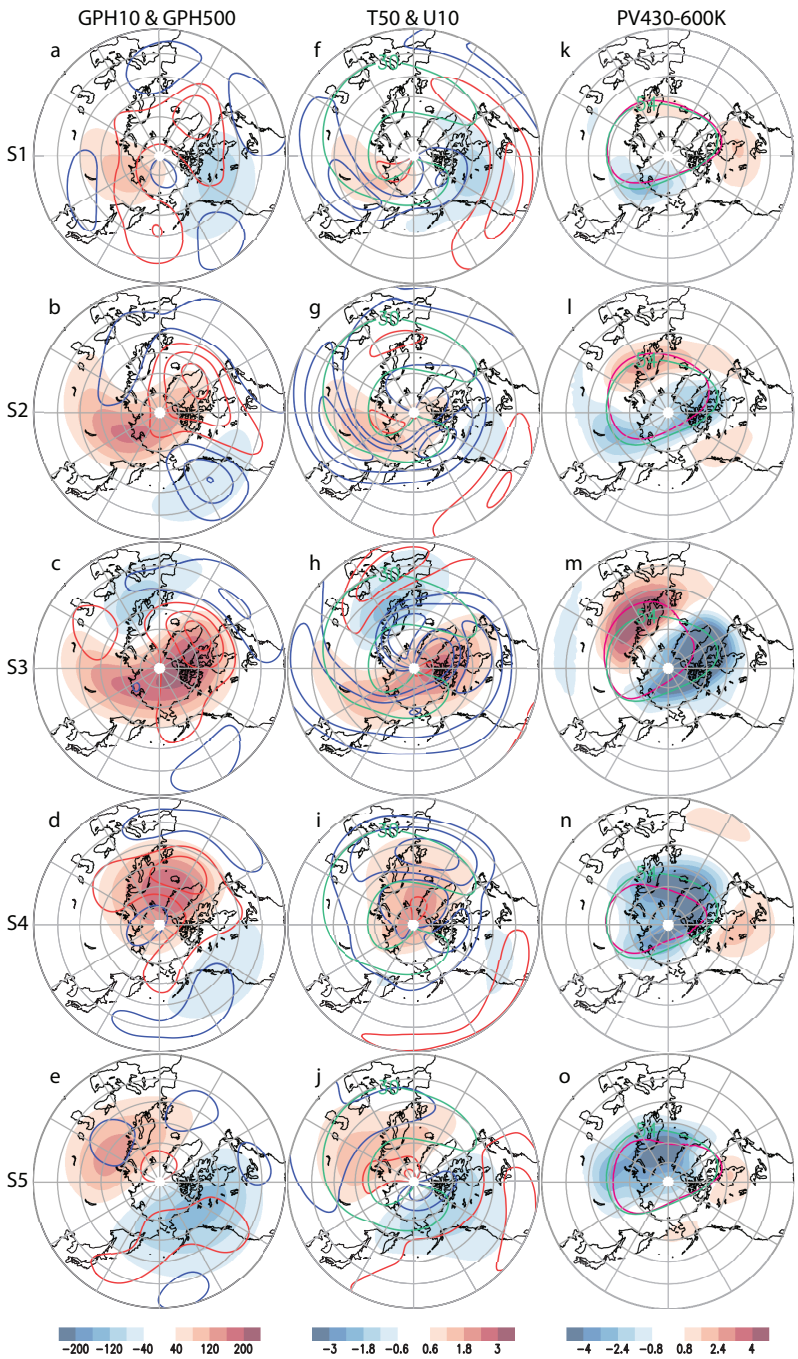

Figure 3.7. Five-stage evolution of (a–e) 10-hPa (shading) and 500-hPa (red (+) and blue (–) contours at ±10, 30, and 50 m) geopotential height anomalies, (f–j) 50-hPa temperature anomalies (shading) and 10-hPa zonal wind (red and blue contours at ±2, 4, and 6 m s^{-1}) with climatological 30 m s^{-1} zonal wind (aqua contour), and (k–o) the vertically averaged (430–600 K) potential vorticity anomalies (shading, 0.8 PVU (10^{-6} K m^2 kg^{-1} s^{-1}) interval) with climatological potential vorticity (aqua contour at 54 PVU) and the perturbed

potential vorticity (magenta contour at 54 PVU) for the second CSEOF mode. The perturbed potential vorticity is obtained by adding the climatology with the 2σ values of the anomalous potential vorticity. Each pattern represents a 17-day average based on the development of positive PCH anomaly at 10 hPa with its maximum in stage 3.

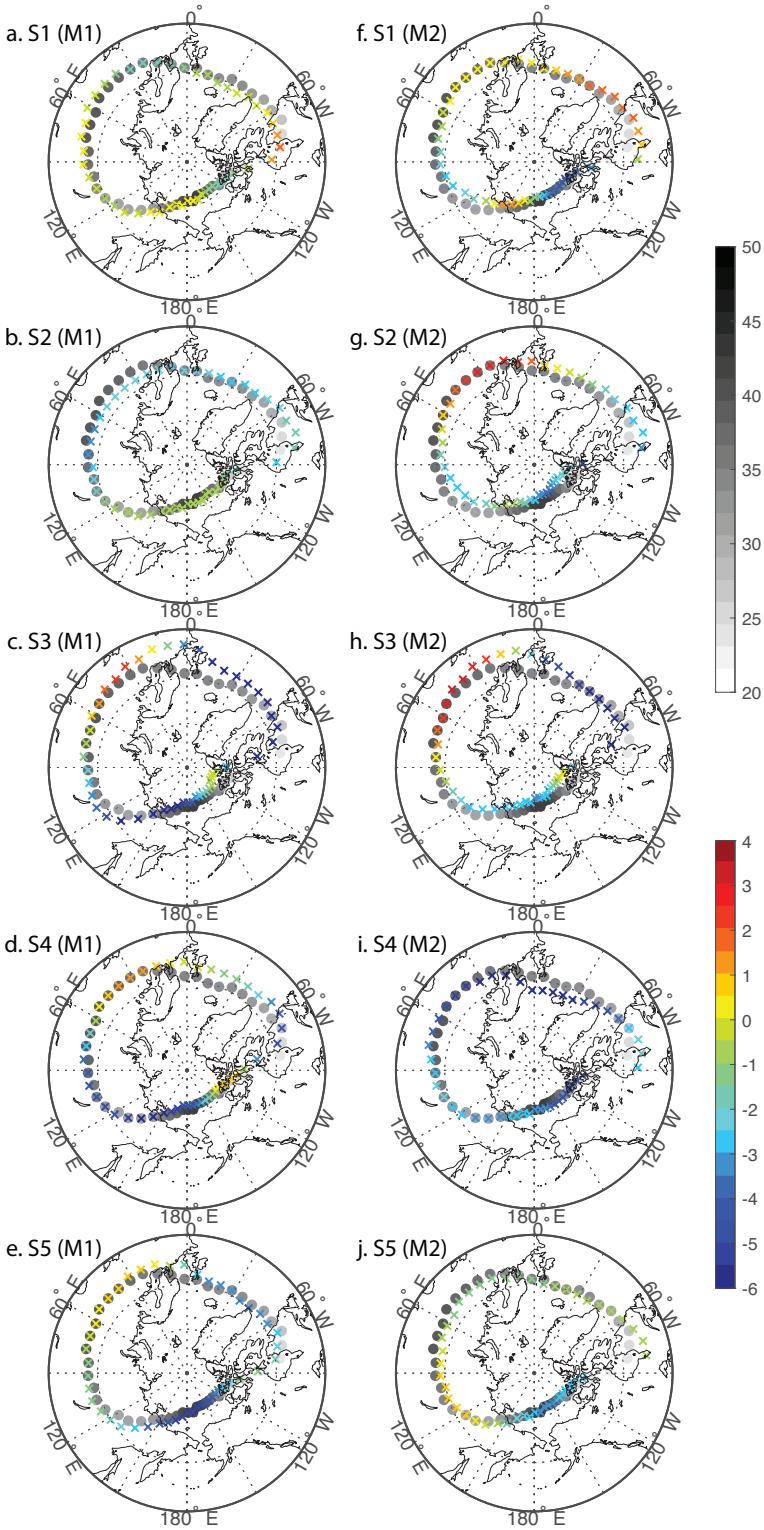
a. S1 (M1)
f. S1 (M2)
b. S2 (M1)
g. S2 (M2)
c. S3 (M1)
h. S3 (M2)
d. S4 (M1)
i. S4 (M2)
e. S5 (M1)
j. S5 (M2)
0°
60° E
60° W
120° E
120° W
180° E
50
45
40
35
30
25
20
4
3
2
1
0
-1
-2
-3
-4
-5
-6

Figure 3.8. Five-stage evolutions of 10-hPa climatological zonal wind maximum (filled circle) and perturbed zonal wind maximum (cross) at each longitude grid in the (a–e) first and (f–j) second CSEOF modes. Symbols are located at every five longitude grids. The color of the cross symbol indicates the degree to which the perturbed field deviates from the climatological field. Each pattern represents (a–e) an 11-day average for the first mode and (f–j) a 17-day average for the second mode, as shown in Figures 3.6 and 3.7.

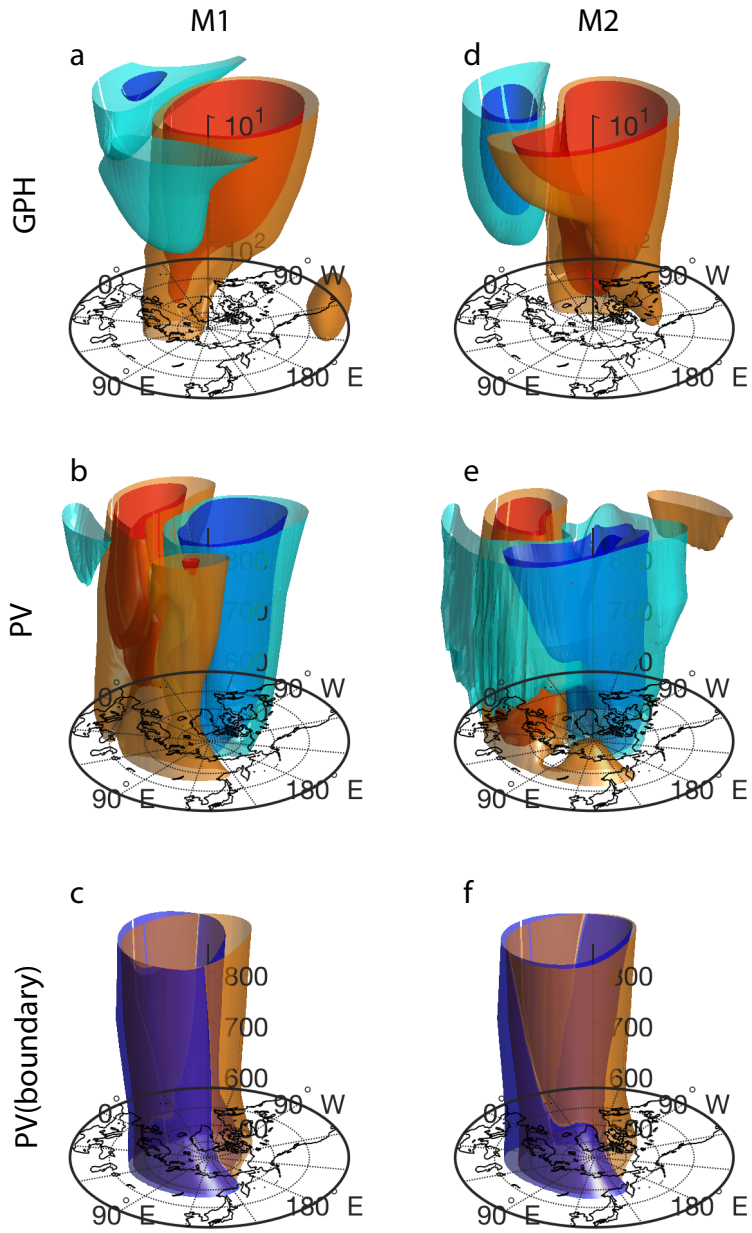

Figure 3.9. Three-dimensional isosurfaces of (a and d) geopotential height anomalies (red: positive, blue: negative, $\pm 35, 70$ m) in pressure levels 500–10 hPa, and (b and e) scaled potential vorticity anomalies ($\pm 2.5, 5 \times 10^{-2}$), (c and f) climatological vortex boundary (yellow) and perturbed vortex boundary (blue) in potential temperature levels 430–850 K for stage 3 of the (a–c) first mode and (d–f) second mode. The perturbed potential vorticity is obtained by adding the climatology with the 2σ values of the anomalous potential vorticity. Each pattern represents (a–c) an 11-day average for the first mode and (d–f) a 17-day average for the second mode, as shown in Figures 3.6 and 3.7.

3.4. Contribution to actual stratospheric vortex fluctuations

The stratospheric polar vortex fluctuations associated with the two leading modes of sea ice are compared with the total vortex variability based on the PCH index which is a proxy for the Northern Annular Mode (NAM) index (Baldwin and Thompson 2009). Reconstructed data based on the two SIC modes accounts for approximately 6 (14) % of the total variance of the PCH index at 10 (100) hPa. SIC-related vortex variability partially accounts for long-term changes in total variability in the lower stratosphere (100 hPa) (lower panel in Fig. 3.10) but less correlated with interannual vortex variability (Fig. 3.10). The results imply that SIC-related vortex variability is relatively small compared to the internal variability of stratospheric vortex deviated from the major SIC variability.

While the contribution of SIC-related variability to the total stratospheric vortex variability is relatively small, an important finding is that their contributions to the low frequency change in stratospheric vortex are different. Both modes exhibit long-term upward trends in terms of stratospheric vortex weakening, but their relative dominance varies in time (Fig. 3.10).

During the 1980–2000s, period of an upward phase transition in the SIC dipole mode, on average, the attenuation of the stratospheric vortex increased in early winter with increased SIC in the Labrador Sea and decreased SIC in the Barents-Greenland Seas (Fig. 3.11b and blue line in Fig.

3.11e). Since the mid-2000s when SIC in the BKS rapidly decreased due to an acceleration of Arctic warming, on the other hand, weakening of the stratospheric vortex in late winter has amplified and has become more frequent compared to previous decades (Fig. 3.11a and red line in Fig. 3.11e). Also, height increases in the high-latitude Pacific and North America region during P1–P2 (Fig. 3.11c) similar to the first mode (Fig. 3.6c) in spatial structure, and height increases in Siberia and Baffin Bay during P3–P4 (Fig. 3.11d), similar to the second mode (Fig. 3.7c).

Similarity between the stratospheric vortex evolution associated with the SIC modes and the long-term change in stratospheric vortex evolution means that the two SIC modes contribute at least partially to long-term change of stratospheric vortex. It is necessary to pay attention to the relative contributions of long-term climate change and natural variability of SIC to better understand inter-decadal change in stratospheric vortex.

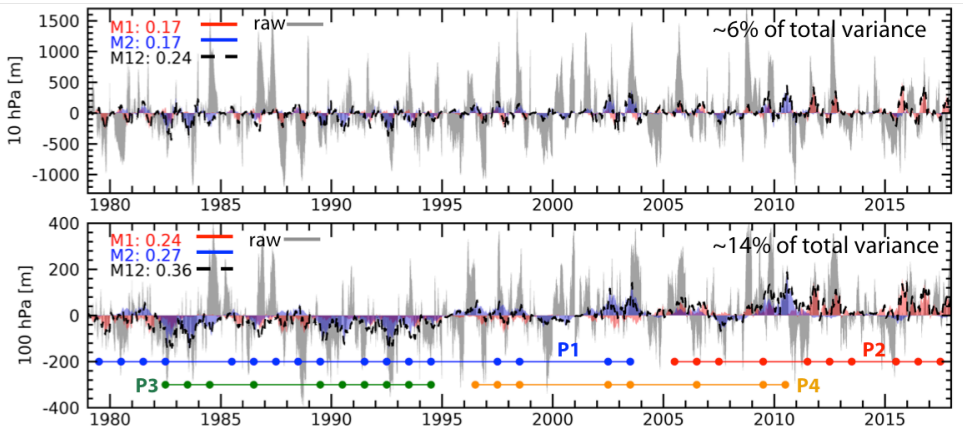

Fig. 3.10. Polar cap averaged [0°–360°E, 65°–87°N] geopotential height (PCH) anomalies from the reconstructed data based on the two SIC modes (black line; red shading: first mode; and blue shading: second mode) and those from the raw data (grey shading) at (upper) 10 hPa and (lower) 100 hPa levels during the data period (1979–2018). The blue (green) and red (orange) lines correspond to the sign (negative and positive, respectively) of the low-frequency amplitude of PCH for the first (second) mode. The circle symbols indicate the years of the same sign in the low frequency phase, and they are used to extract the composite patterns associated with the first two modes as in Fig. 3.11.

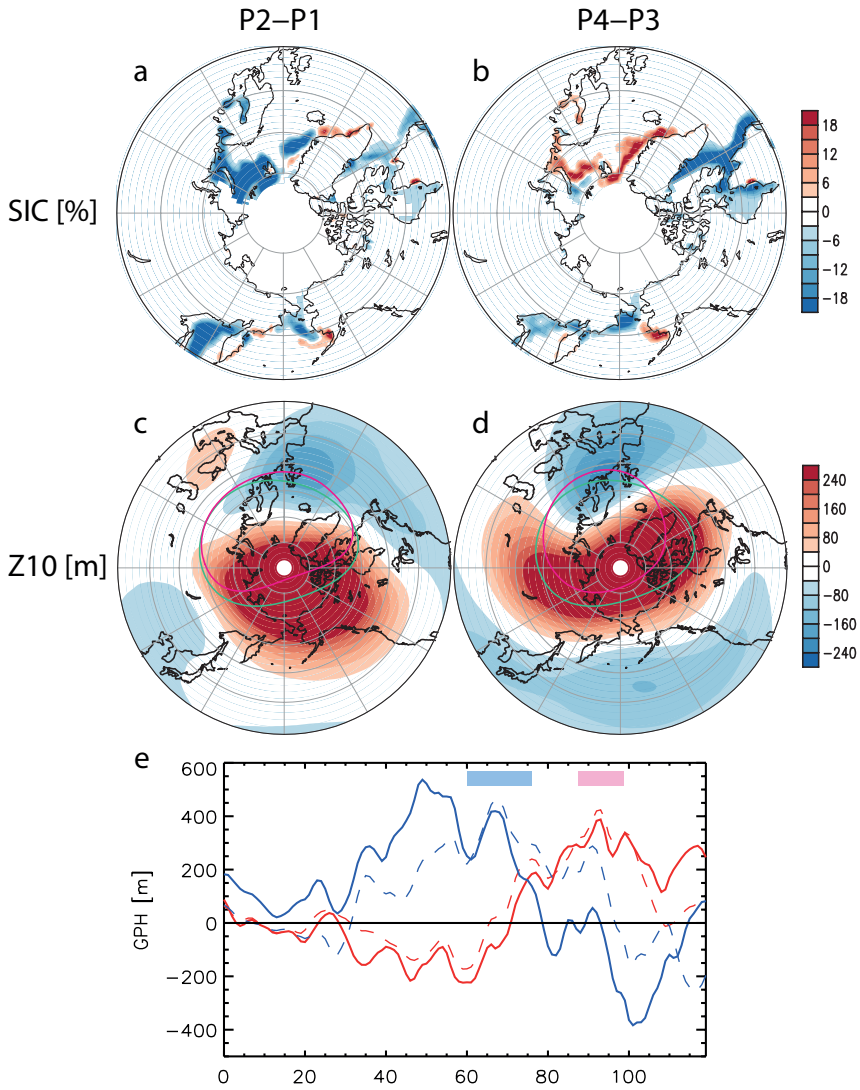

Fig. 3.11. (a and b) Composite mean differences of sea ice anomalies and (c and d) of 10-hPa geopotential height anomalies between the positive and the negative PCH amplitude marked in Fig. 3.10 for (a and c) the P1 and P2 periods (P2–P1) and (b and d) the P3 and P4 periods (P4–P3). The perturbed vortex boundary (aqua contour at 29,870 m) is shown in comparison with the climatological vortex boundary (magenta contour at 29,870 m). (e) Composite mean difference of 10-hPa polar cap averaged geopotential height anomalies from the raw data (solid) and that from the reconstructed data based on the first (red dashed) and the second (blue dashed) SIC modes between the periods P2 and P1 (red), and P4 and P3 (blue). Patterns in (a) and (c) represent 11-day averages around the mature phase in 10-hPa PCH anomaly (pink bar in e) for the first mode. Patterns in (b and d) represent 17-day averages around the mature phase (blue bar in e) of the second mode.

Chapter 4. Stratosphere-troposphere variability in connection with the leading modes of NH tropopause variability

In previous chapter, the temporal and geographical evolutionary features of stratospheric polar vortex for two major modes of Arctic sea ice variations were investigated: Arctic sea ice reduction and North Atlantic dipole sea ice variations. The results explain the linkage of sea ice variability to stratospheric polar vortex fluctuations depending on a specific sea ice mode, which can improve the understanding of sea ice-stratospheric vortex relationship under the rapid Arctic surface climate changes.

In this chapter, a more general concept of stratosphere-troposphere coupled variability is dealt with. Results can provide information about the major evolution structures of stratosphere-troposphere variability in association with the leading modes of tropopause variability.

4.1. Leading modes of the NH tropopause pressure variation

a. Evolution patterns of tropopause pressure

The first two leading modes of the tropopause pressure variability in the Northern Hemisphere cold season are characterized by high-latitude signals on sub-seasonal time scales (Figs. 4.1 and 4.2). The first mode accounts for ~12% of the total variance. This mode exhibits a persistent tropopause

depression from winter to early spring; there are strong positive anomalies in the polar region from January to March (Fig. 4.1a–f). The Arctic anomalies develop in an approximately concentric fashion around the North Pole. Weak negative anomalies are developed over the Pacific sector during January–February and weak positive anomalies over the Atlantic sector during February–April.

The second mode explains about 7.7% of the total variance. The second mode indicates winter-spring oscillation of the Arctic tropopause anomalies, which consist of a relatively weak winter signal and a relatively strong spring signal of the opposite sign. Negative anomalies exist in the polar region in December–February with a phase transition in February leading to positive anomalies in March–April (Fig. 4.2a–f). In addition to the development of these Arctic anomalies, local anomalies also develop across the hemisphere. They are particularly apparent in November, December, and February when the Arctic signal is not so strong or is in the stage of phase transition.

The PC time series corresponding to each mode shows a large interannual variation in both modes (Figs. 4.1g and 4.2g). The correlation coefficients between the two PC time series are generally insignificant within the lag of ±72 pentads ($-0.19 < r < 0.04$) (figure not shown); this suggests that the two leading modes are statistically independent and are derived from different physical processes. The PC time series of the first mode is weakly correlated with interannual variation of the Arctic Oscillation (AO) (–0.41 with the ±17-pentad smoothed AO index). This paper deals with the variations

of other physical variables corresponding to the positive phase of the PC time series in Figs. 4.1g and 4.2g. For the negative phase, the results are the same except for the opposite signs.

Results in this section show that the two leading CSEOF modes of tropopause pressure variability are characterized by zonally asymmetric signals dominant in the Arctic. The first mode represents a strong increase in tropopause pressure in the Arctic, lasting from January to March. The second mode shows a relatively weak reduction of tropopause pressure in December–February and a relatively strong increase in March–April.

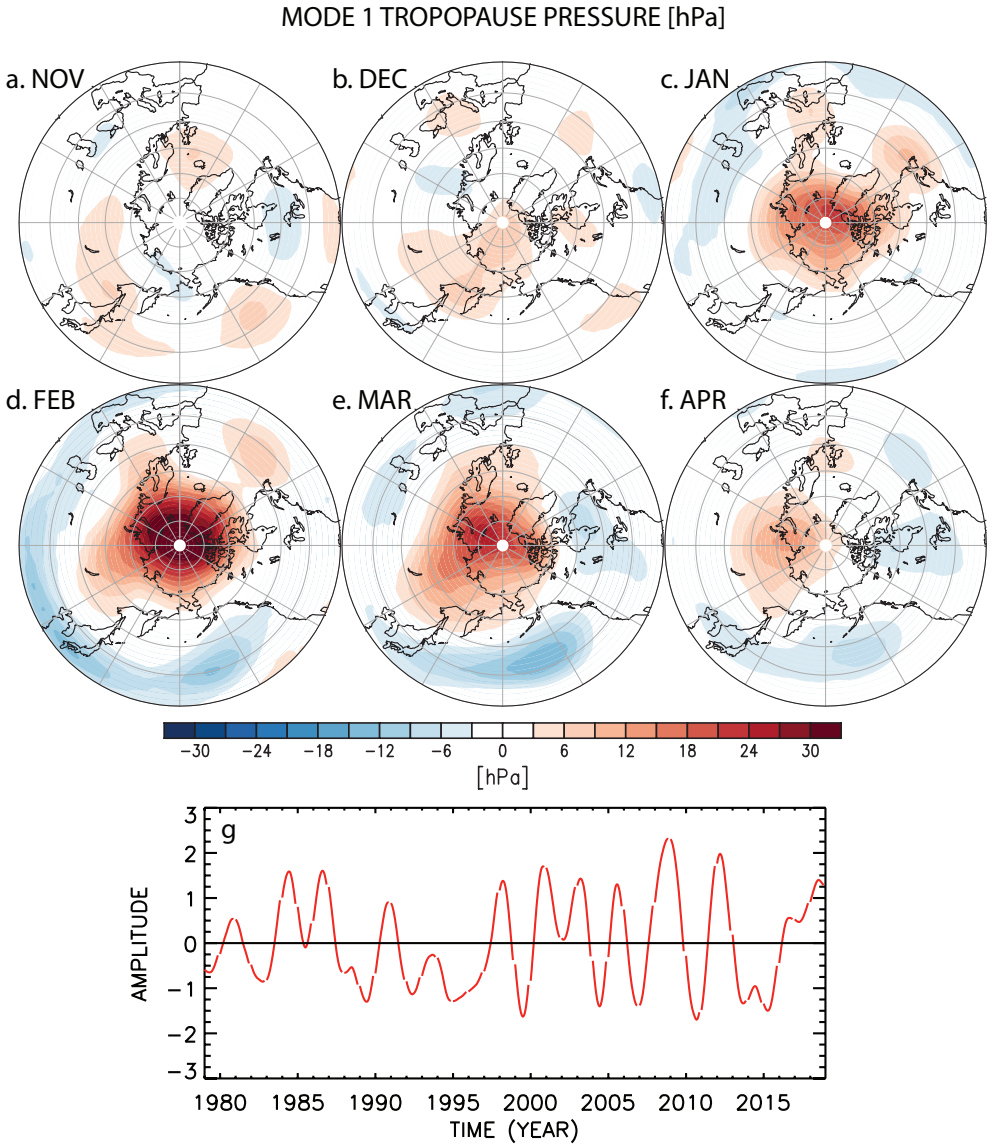

Figure 4.1. (a–f) Monthly mean loading vectors for the first CSEOF mode of the tropopause pressure variability [hPa] and (g) corresponding principal component time series.

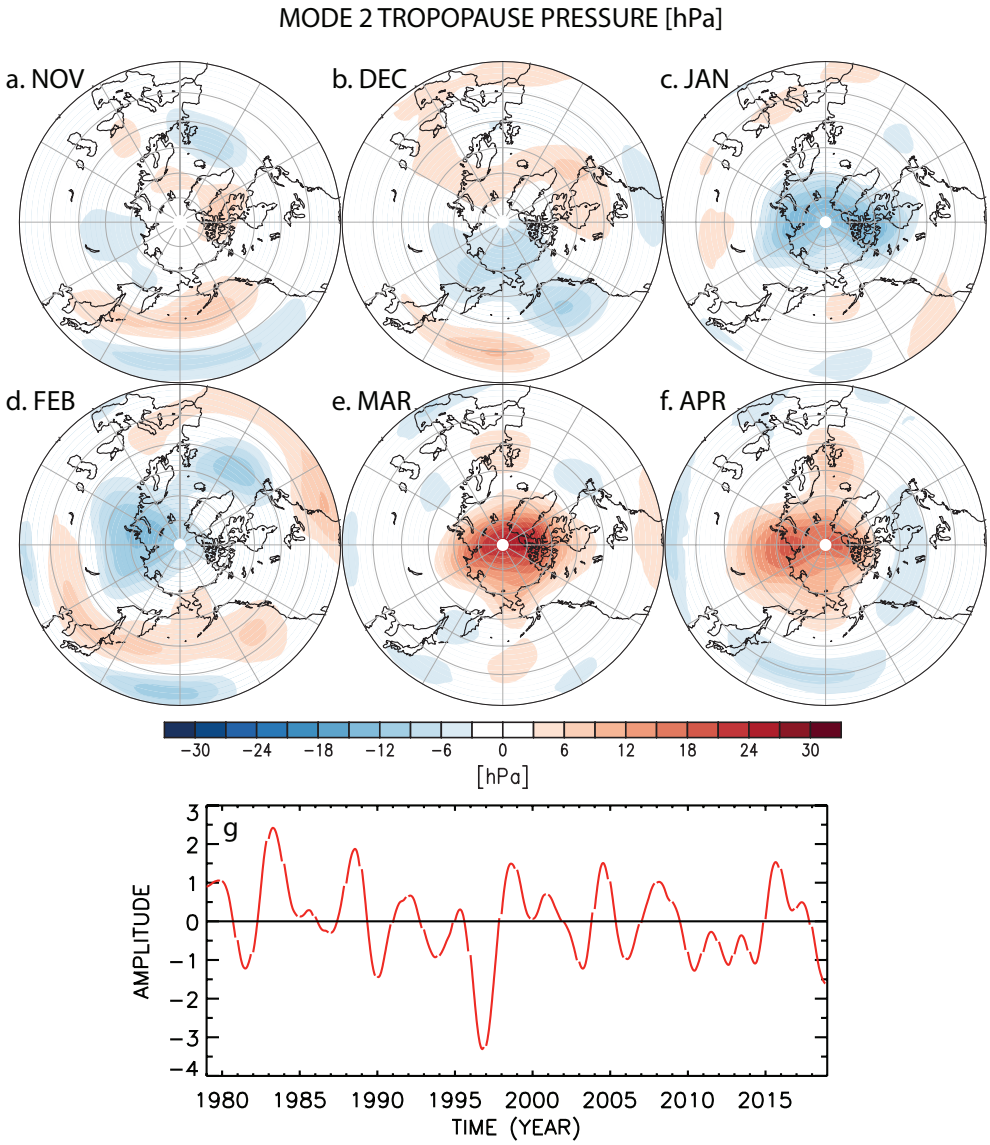

Figure 4.2. (a–f) Monthly mean loading vectors for the second CSEOF mode of the tropopause pressure variability [hPa] and (g) corresponding principal component time series.

b. Sensitivity test on the choice of tropopause variables

In this study, tropopause pressure from NCEP reanalysis product is used to analyze major modes of tropopause variability. This tropopause data is based on lapse-rate criterion. The tropopause is the lowest level at which the lapse rate decreases to 2°C/km or less, and this level also should satisfy the condition that the average lapse rate between this level and all higher levels within 2 km does not exceed 2°C/km (WMO, 1957). However, there is another definition of tropopause, which is based on a particular PV isosurface. The threshold value is generally chosen between 1.5 to 4 PVU (1 PVU = 10^{-6} K kg^{-1} m^2 s^{-1}) (Baldwin et al. 2019). In addition, there are also several tropopause parameters, such as pressure, temperature, and height. Therefore, to confirm the robustness of the results in the previous section, first two modes of tropopause variability have been reproduced using other tropopause variables. Figures 4.3 and 4.4 show the loading vectors derived from the lapse-rate tropopause pressure and temperature from NCEP reanalysis product, the lapse-rate tropopause pressure from ERA interim reanalysis product, and the pressure and geopotential height at the 2 PVU level from ERA5 reanalysis product. The lapse-rate tropopause pressure from ERA interim reanalysis is obtained from vertical temperature profiles by using the method of Reichler et al. (2003). The 2 PVU isosurface is considered as dynamical tropopause (Baldwin et al. 2019).

Similar evolution patterns are found in the five tropopause variables, except that patterns of pressure and geopotential height at 2PVU level are

more localized and complicated (Figs. 4.3 and 4.4). This difference may be related to the fact that the altitude of the 2 PVU isosurface is lower than that of the lapse-rate tropopause, which means that synoptic scale tropospheric variability is more involved. Their PC time series also show similar interannual variation to each other except for the geopotential height at the 2PVU level (Fig. 4.5). This comparison suggests that the results are not qualitatively very sensitive to the choice of the tropopause variables or datasets.

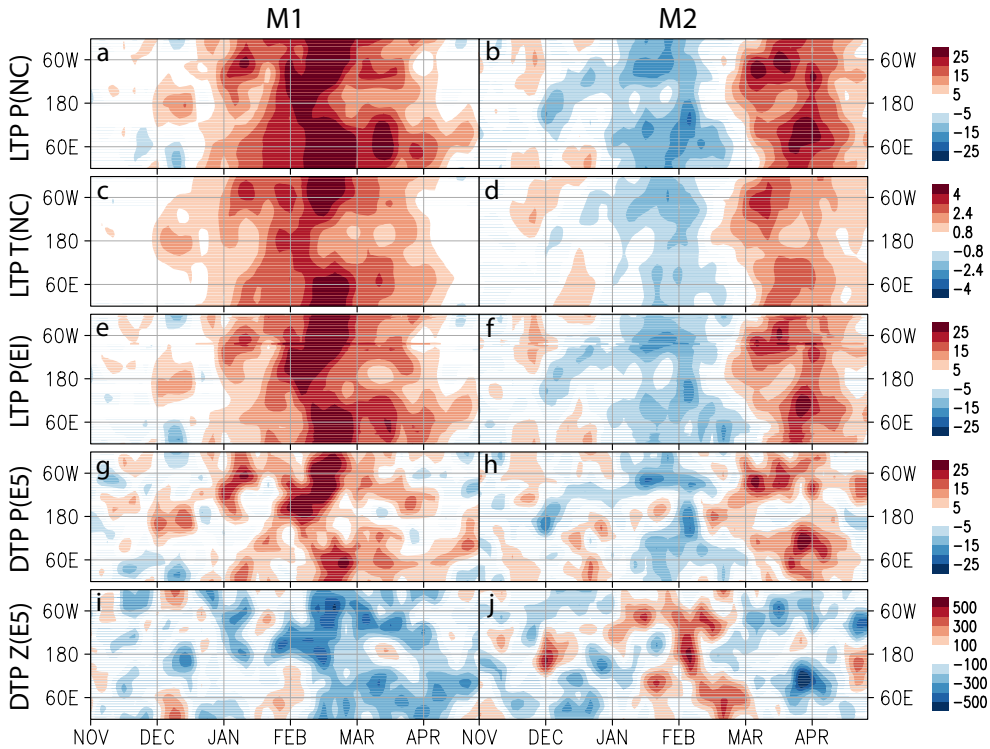

Figure 4.3. Time-longitude tropopause anomalies of the two CSEOF leading modes depending on the different tropopause variables in high latitude (75°–85°N): lapse-rate tropopause (LTP) (a and b) pressure and (c and d) temperature from NCEP reanalysis data, (e and f) lapse-rate tropopause pressure from ERA interim reanalysis data, and (g and h) pressure and (i and j) geopotential height at 2PVU level as a proxy of dynamical tropopause (DTP) from ERA5 reanalysis data.

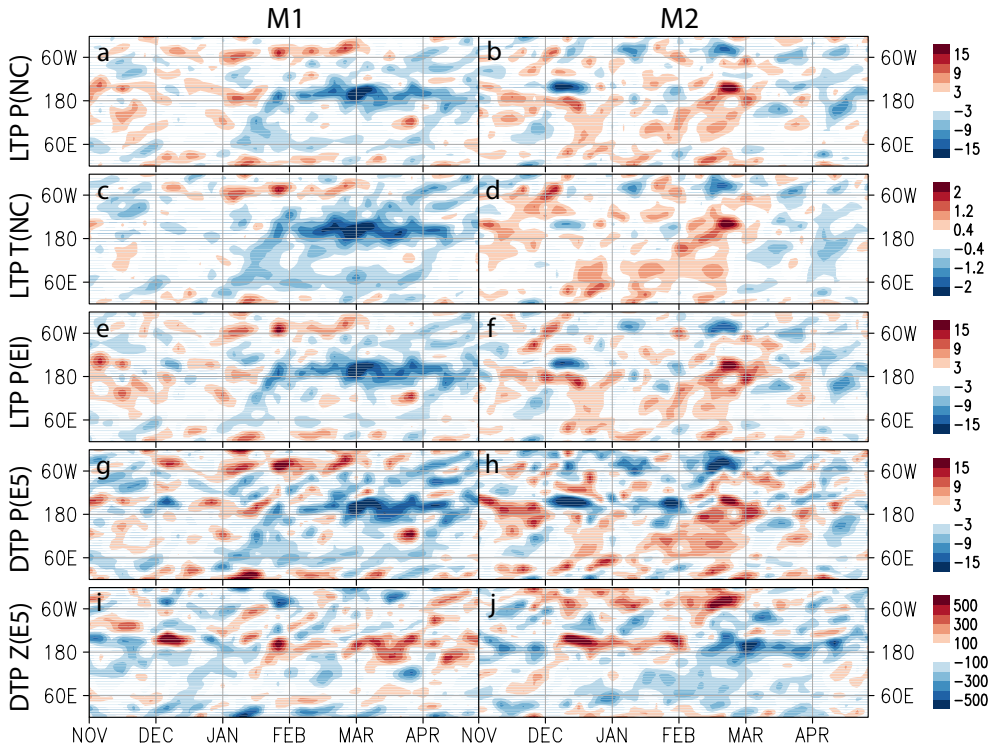

Figure 4.4. Time-longitude anomalies of the two CSEOF leading modes depending on the different tropopause variables in mid latitude (40°–50°N): lapse-rate tropopause (LTP) (a and b) pressure and (c and d) temperature from NCEP reanalysis data, (e and f) lapse-rate tropopause pressure from ERA interim reanalysis data, and (g and h) pressure and (i and j) geopotential height at 2PVU level as a proxy of dynamical tropopause (DTP) from ERA5 reanalysis data.

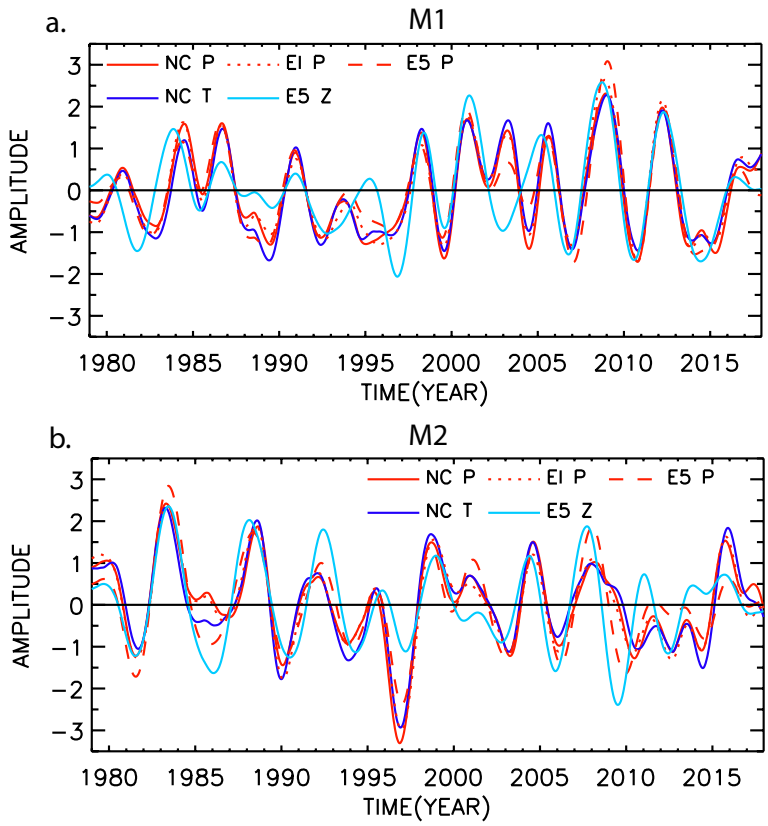

Figure 4.5. PC time series of first two CSEOF modes depending on the different tropopause variables: lapse-rate tropopause pressure (NC P, red solid) and temperature (NC T, blue solid) from NCEP reanalysis data, lapse-rate tropopause pressure (EI P, red dotted) from ERA interim reanalysis data, and pressure (E5 P, red dashed) and geopotential height (E5 Z, light blue solid) at 2PVU level as a proxy of dynamical tropopause from ERA5 reanalysis data.

4.2. Evolution in the Arctic stratosphere and troposphere and its linkage to the Arctic tropopause variability from a zonal mean perspective

Based on the lapse-rate definition, tropopause pressure (height) is closely related to changes in the vertical gradient of temperature in the upper troposphere and lower stratosphere (UTLS) (shading in Fig. 4.6), i.e. changes in static stability such as the square of buoyancy frequency (Seidel and Randel 2006; Wang et al. 2016). In the Arctic region, tropopause anomalies are dominantly affected by stratospheric temperature anomalies and are more closely related to stratospheric zonal wind anomalies than to tropospheric anomalies (Fig. 4.6). Thus, a rise in Arctic tropopause pressure is largely due to an increase in the stratospheric temperature and the UTLS static stability, and is accompanied by a weakening of stratospheric westerlies that satisfy the thermal wind balance (Fig. 4.7). Conversely, a reduction in tropopause pressure is accompanied by a decrease in stratospheric temperature and UTLS static stability, and a strengthening of stratospheric westerlies. This relationship is similar to the results in other studies (Ambaum and Hoskins 2002; Barroso and Zurita-Gotor 2016; Tomassini et al. 2012; Jucker 2016; Wong and Wang 2003; Zängl and Hoinka 2001).

In the first mode, temperature begins to increase in the polar stratosphere from early December, and then tropopause pressure begins to rise near the end of December. Strong temperature anomalies (see e.g., 1.5°C contour line) gradually grow and descend for about two months (Fig. 4.7a).

The signal peaks in mid-February and persists until early April in the lower stratosphere. This increase in temperature indicates a weakening of the cold stratospheric polar vortex. In association with the positive temperature anomalies, negative static stability anomalies develop above them and positive static stability anomalies develop near the tropopause (shading in Fig. 4.7b). It seems that the stratospheric warming and a subsequent increase in static stability near the tropopause result in a rise in tropopause pressure (shading in Fig. 4.7a and b). The positive static stability anomalies near the tropopause also explain positive PV anomalies there (contours in Fig. 4.7b). Change in PV near the tropopause is dominated by the static stability component than the absolute vorticity component (figure not shown). Anomalous tropospheric cooling develops from February (Fig. 4.7a). This tropospheric cooling can further intensify the tropopause pressure increase induced by stratospheric warming.

The development of the positive temperature anomalies is linked thermodynamically with that of negative zonal wind anomalies (Fig. 4.7c). This change in zonal mean zonal wind is attributable to the variation of the Eliassen-Palm (EP) flux divergence (shading in Fig. 4.7d) (Baldwin and Dunkerton 2001; Polvani and Waugh 2004; Thomson and Wallace 2000), which is dominated by the vertical component of EP flux anomalies (contours in Fig. 4.7d). Similar to the positive temperature anomalies, negative zonal wind anomalies develop in the upper stratosphere from early December (Fig. 4.7c). This is related to prominent upward EP flux anomalies throughout the troposphere and stratosphere and their convergence in the stratosphere

during late November–mid-February (Fig. 4.7d). The bottom level of the anomalous convergence seems to descend toward the tropopause, which is consistent with the downward expansion of the zonal mean stratospheric easterly (Limpasuvan et al. 2004; 2005) (Fig. 4.7d). In February–April, downward flux and divergence of EP flux anomalies are dominant in the stratosphere. They are related to a reduction in the anomalous easterly wind and a subsequent phase transition to the anomalous westerlies in the stratosphere.

In the second mode, negative temperature anomalies first appear from the upper stratosphere in early December and change to positive anomalies during February (Fig. 4.7e). The UTLS static stability and tropopause pressure display negative anomalies from the end of December and positive anomalies from the end of February (shading in Fig. 4.7f). PV anomalies near the tropopause also show evolution similar to the tropopause pressure anomalies (contours in Fig. 4.7f). The spring phase with a peak in March is relatively strong compared to the winter phase with a peak in January. The evolution of the second mode exhibits a shorter duration of about 2 months and a half and a faster growth and a shorter descending time scale of about 1 month for each phase compared to the first mode (Fig. 4.7a and e). The second mode describes a strengthening of the cold stratospheric polar vortex in winter and a weakening in spring.

Together with the negative and positive temperature anomalies, positive and negative zonal wind anomalies appear in the stratosphere (Fig. 4.7g). The evolution of the vertical EP flux anomalies and divergence with

alternating signs in the stratosphere coincide with the variation of zonal mean flow (Fig. 4.7h). The direction of the vertical EP flux anomalies in the stratosphere is opposite to that in the troposphere during December–January, but the direction thereafter is the same throughout the stratosphere and troposphere (contours in Fig. 4.7h). Vertical EP flux anomalies are mainly explained by zonal wavenumber-1 component in both modes (figure not shown). Zonal wavenumber-2 component of vertical EP flux anomaly has the same signs as the zonal wavenumber-1 component in the first mode, but has the opposite signs in the second mode.

In both modes, the anomalous zonal mean flow started from the upper stratosphere is clearly traced in the troposphere; evolution coherent in phase appears in the troposphere (contours in Fig. 4.8a and d and Fig. 4.9). In connecting the zonal mean flow in the stratosphere and that in the troposphere, variation of eddy momentum flux seems to play an important role (Limpasuvan et al. 2004; Simpson et al. 2009). This momentum flux is negatively proportional to the meridional component of EP flux. In the first mode, when anomalous easterlies occupy the lower stratosphere, northward EP flux is dominant in the upper troposphere (shading in Fig. 4.8a). The northward EP flux corresponds to southward eddy momentum flux, which decelerates the zonal mean flow in higher latitudes and accelerates the zonal mean flow in lower latitudes. This anomalous eddy momentum forcing is consistent with easterly wind anomalies in the polar region (contours in Fig. 4.8a). Along with these momentum flux anomalies, Eulerian mean meridional circulation develops, which consists of anomalous northward wind in the

upper troposphere, anomalous southward wind in the lower troposphere (shading in Fig. 4.8b) and anomalous downward motion in the Arctic region (contours in Fig. 4.8b). Coriolis force acting on the meridional wind anomalies induces westerly momentum in the upper troposphere and easterly momentum in the lower troposphere (shading in Fig. 4.8b). In the perspective of momentum balance, the westerly wind anomaly driven by Coriolis force in the upper troposphere attenuates the easterly wind anomaly driven by divergence of momentum flux anomaly (shading in Fig. 4.8a and b). On the other hand, in the lower troposphere, the easterly wind anomaly driven by Coriolis force is partially offset by surface friction. Therefore, eddy momentum forcing as well as related mean meridional circulation play a crucial role in the evolution of tropospheric zonal wind anomaly with the same polarity as the high-latitude stratospheric zonal wind anomaly (Limpasuvan et al. 2004; Simpson et al. 2009). These relationships can also be seen in the second mode (Fig. 4.8d and e). When anomalous westerly prevails in the lower stratosphere during winter, southward EP flux anomalies are dominant in the upper troposphere (shading in Fig. 4.8d). They are accompanied by anomalous southward winds in the upper troposphere, anomalous northward winds in the lower troposphere (shading in Fig. 4.8e), and anomalous upward motion in the Arctic region (contours in Fig. 4.8e). As anomalous easterly develops in the stratosphere in spring, anomalous meridional EP flux and associated anomalous mean meridional circulation are reversed.

The zonal-mean zonal wind variations in the subpolar region coincide with the polar cap averaged geopotential height (PCH) variations in the lower

troposphere (bars in Fig. 4.8c and f). PCH anomalies show more complicated fluctuations than the tropopause anomalies (black line in Fig. 4.8c and f), which are directly affected by the low-frequency change in the lower stratospheric temperature. In the first mode, while the tropopause pressure increases, PCH increases along with easterly anomalies in the troposphere (Fig. 4.8a and c). The northward EP flux anomalies peak at the end of January, and become relatively weak in February–early March. However, the intensity of the positive height anomalies tends to be maintained during this period. This may be partly related to the tropospheric column compression effect due to the tropopause height decrease: a reduction in the height of the tropospheric column as a result of stratospheric warming reduces relative vorticity below, which is associated with an increase in surface pressure (Ambaum and Hoskins 2002; Tomassini et al. 2012) (Fig. 4.9). The relationship between the stratospheric polar easterly anomaly and the positive anomalies in the tropopause pressure and near-surface geopotential height can also be explained in terms of global mass circulation (Cai and Ren 2007; Kidston et al. 2015). Convergence of EP flux anomalies associated with the stratospheric polar easterly anomaly induces a strengthening of the residual meridional circulation. As a result, anomalous air inflow and descending motion above the polar region increase tropopause pressure and surface pressure.

In the second mode, like the tropopause pressure fluctuation, tropospheric PCH exhibits negative winter anomalies followed by positive spring anomalies (bars in Fig. 4.8f). However, tropopause and tropospheric

PCH anomalies evolve differently in the detail (black line in Fig. 4.8f). In the winter phase, negative anomalies of PCH develop and decline more rapidly than the anomalous tropopause pressure. On the other hand, positive anomalies of PCH last longer than the anomalous tropopause pressure in the spring phase.

The main point of this section is that the two modes of tropopause pressure are strongly linked to changes in stratospheric polar vortex strength and are coupled with coherent evolution throughout the stratosphere and troposphere in the Arctic. In other higher modes, tropopause anomalies are less correlated with upper-middle stratospheric variations (figure is not shown), and surface pressure anomalies evolve differently from the anomalies related to stratospheric and tropopause fluctuations (Fig. 4.9). That is, the downward effect of the upper stratospheric vortex fluctuations tends to be relatively weak in other higher modes. This means that stratosphere-troposphere coupled variability with vertically coherent evolution is tied with the two tropopoause modes.

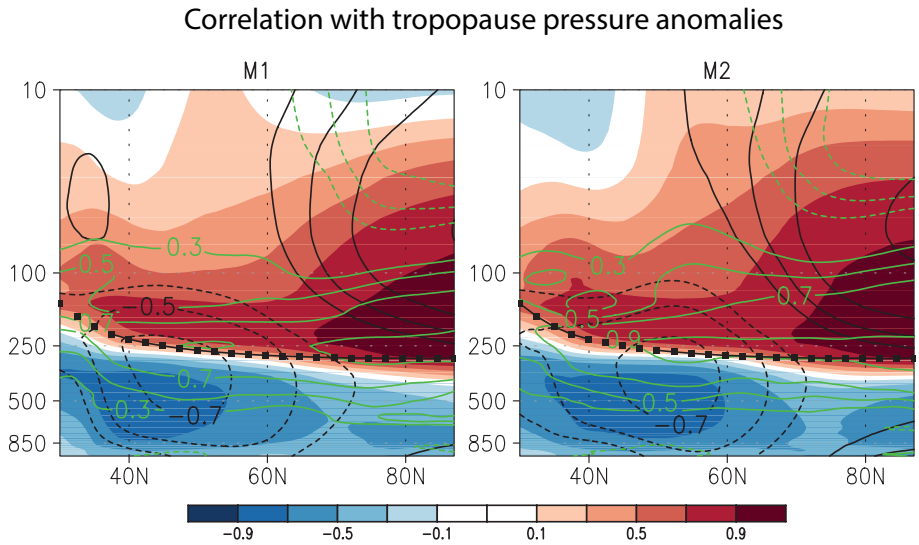

Figure 4.6. Zonal averaged correlation of tropopause pressure anomalies with air temperature anomalies (shading), geopotential height anomalies (black contours, ±0.3, 0.5, 0.7 and 0.9) and potential vorticity anomalies (green contours, ±0.3, 0.5, 0.7 and 0.9) for (left) the first and (right) the second CSEOF modes of tropopause variability. The climatological tropopause elevation is shown as a black dotted line.

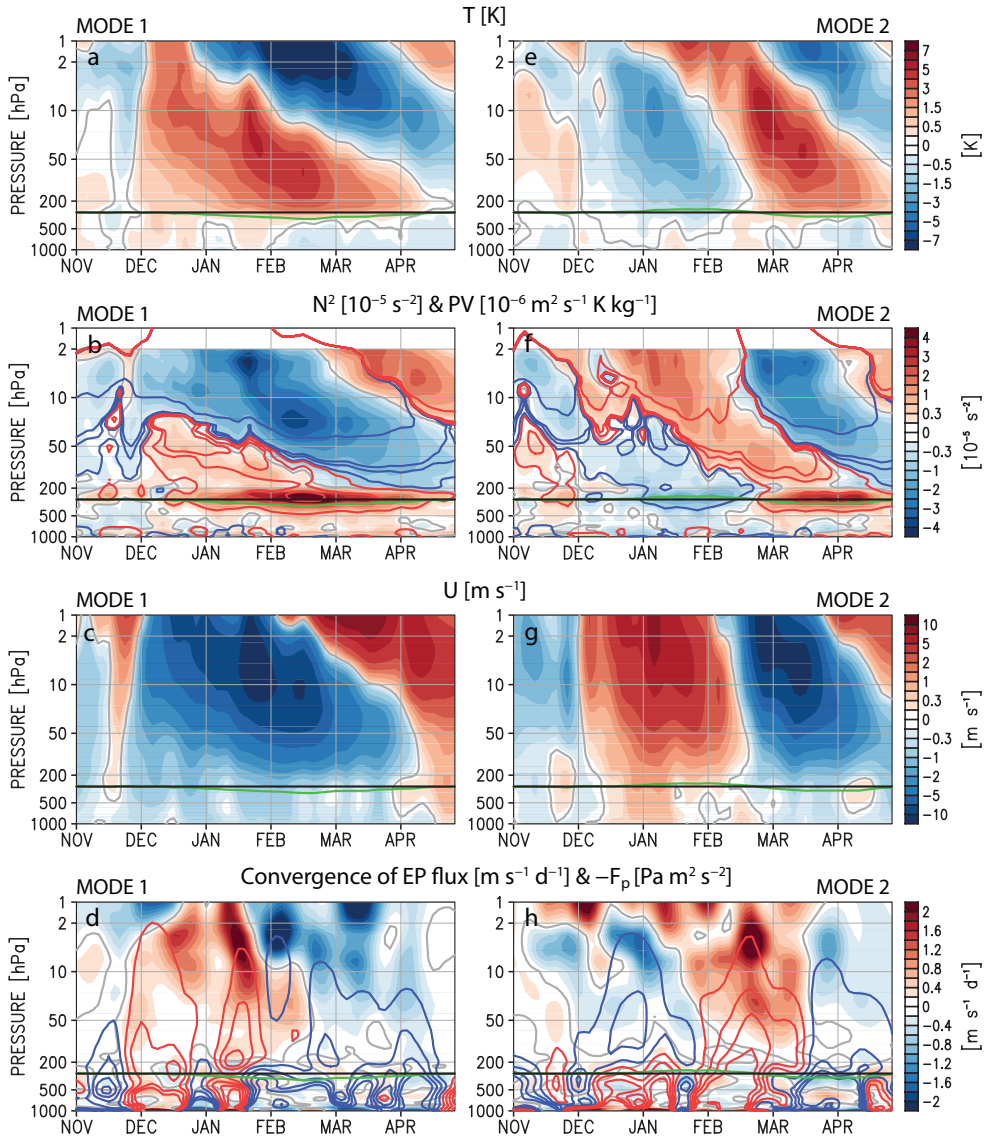

Figure 4.7. Time-altitude zonal mean patterns of (**a** and **e**) 65°–87°N averaged air temperature anomalies [K], (**b** and **f**) 65°–87°N averaged static stability anomalies [shading, 10^{-5} s^{-2}] and potential vorticity anomalies [red (+) and blue (–) contours at ± 0.05, 0.3, 0.5, and 5 PVU (10^{-6} m^2 s^{-1} K kg^{-1})], (**c** and **g**) 50°–80°N averaged zonal wind anomalies [m s^{-1}], and (**d** and **h**) 50°–80°N averaged convergence of EP flux anomalies [shading, m s^{-1} day^{-1}] and vertical EP flux anomalies [red (upward) and blue (downward) contours at ± 0.5, 1.5, 2.5, and 3.5 × 10^5 Pa m^2 s^{-2}] and tropopause fluctuations (green line) for the (**a**–**d**) first and (**e**–**h**) the second CSEOF modes of tropopause variability. The tropopause fluctuation is obtained by adding the 3σ values of the anomalous field to the climatology. The grey line depicts the zero contour of the shaded anomalies.

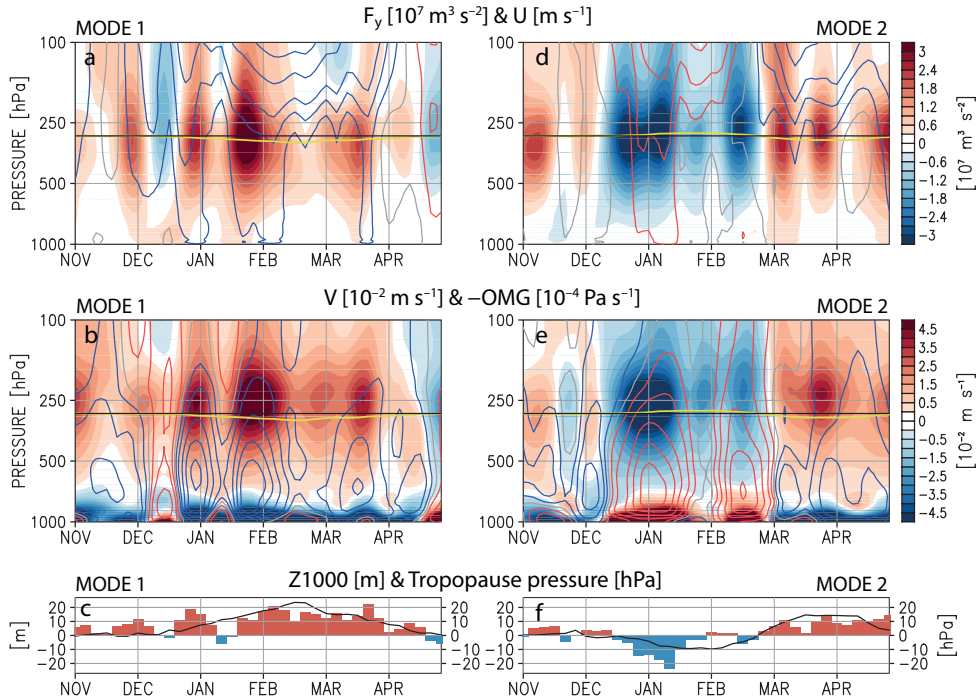

Figure 4.8. Time-altitude zonal mean patterns of (**a** and **d**) 40°–70°N averaged meridional EP flux anomalies [shading, 10^7 m^3 s^{-2}] and 50°–80°N averaged zonal wind anomalies [red (+) and blue (–) contours at ± 0.5, 1.5, 2.5, and 3.5 m s^{-1}], (**b** and **e**) 50°–80°N averaged meridional wind anomalies [shading, 10^{-2} m s^{-1}] and 65°–87°N averaged vertical (–ω) wind anomalies [red (upward) and blue (downward) contours at ± 2, 5, 10, 15, and 20 × 10^{-4} Pa s^{-1}], tropopause fluctuations (yellow line), (**c** and **f**) 65°–87°N averaged geopotential height anomalies [color bar, m] at 1000 hPa and tropopause pressure anomalies [black line, hPa] for the (**a**–**c**) first and (**d**–**f**) the second CSEOF modes of tropopause variability. The tropopause fluctuation is obtained by adding the climatology with a 1σ value of the anomalous field. The grey line depicts the zero contour of the contoured anomalies.

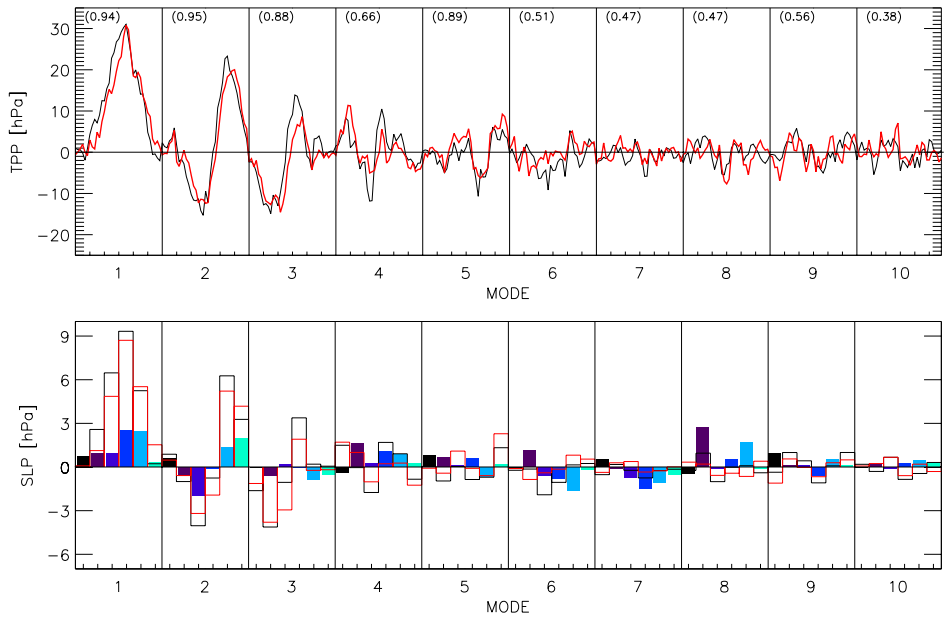

Figure 4.9. (upper panel) Temporal evolution of the Arctic averaged tropopause pressure anomalies (TPP) (red) and PV induced tropopause pressure anomalies (PV-TPP) (black) for the first ten CSEOF modes. The values in parentheses are the correlation coefficients of the two time series in each mode. (lower panel) Arctic averaged sea level pressure anomalies (color bar for each month), PV-TPP induced sea level pressure (black) and TPP induced sea level pressure (red) for the first ten CSEOF modes of tropopause variability; it is calculated using equations relating tropopause pressure and sea level pressure anomalies in Ambaum and Hoskins (2002). Different colors of the color bar indicate each month from November to April.

4.3. Horizontal evolution patterns of the stratospheric and tropospheric circulation

Figures 4.10 and 4.11 depict monthly averaged horizontal evolution of geopotential height and zonal wind anomalies. In the first mode, positive height anomaly develops in the Arctic stratosphere but is slightly shifted to the northern Europe in February, like a climatological stratospheric vortex (shading in Fig. 4.10c). Easterly wind anomaly surrounding the positive height anomaly reduces stratospheric polar jet speed in all sectors. That is, these stratospheric anomalies depict that the stratospheric polar vortex weakens and its center migrates toward the northern Europe, particularly during December–February (green dashed contour in Fig. 4.10a–c). The polar high and easterly anomalies last until March in the lower stratosphere (Fig. 4.10f–j). In February–March, the polar easterly and mid-latitude westerly winds are shifted further south in the North Atlantic and further north in the North Pacific (contours in Fig. 4.10h and i).

In the lower troposphere, anomalous high is observed in the Barents Sea-Ural region during December, which is favorable to enhance upward EP flux of zonal wavenumber 1 and 2 (shading in Fig. 4.10k). With the stratospheric vortex weakening, positive height anomaly appears over Iceland and the Arctic in January (Fig. 4.10l). The Arctic high anomaly is strong until March and the surrounding easterly wind anomaly stays strong in the Atlantic region (shading in Fig. 4.10l–n). Low anomalies seen to the south of the Arctic high anomaly reminds the negative AO/NAO circulation patterns. In the

Pacific sector, however, low anomaly is located at higher latitudes than in a typical AO condition during February and March, and positive height anomaly is dominant in mid-latitudes (shading in Fig. 4.10m and n). This is similar to the tropospheric pattern over the Pacific region during late winter–spring in association with the weakening of stratospheric polar vortex in Zhang et al. (2019). The polar easterly and mid-latitude westerly winds in the Pacific, located further north than in the Atlantic as in the lower stratosphere, are related to these zonally asymmetric height anomalies in mid-latitudes. In addition to a weak correlation between the PC time series and the AO index, the circulation patterns indicate that the first mode contributes, at least partially, to the interannual variation of the AO (or NAO when zonal asymmetry is considered) in January–March.

The winter phase of the second mode shows negative height anomaly in the upper stratosphere, which is centered near the Chukchi Sea (shading in Fig. 4.11a and b). Westerly wind anomaly surrounding the negative height anomaly is relatively weak over Eurasia. Nevertheless, when anomalies are fully developed during January, the climatological stratospheric polar jet accelerates in all sectors (contours in Fig. 4.11b). These polar westerly anomaly and polar low anomaly also appear in the lower stratosphere and the troposphere (Fig. 4.11g and l). In the lower troposphere, positive height anomalies in the Atlantic and northeastern Pacific surrounding the low anomaly is reminiscent of a positive phase of the AO (shading in Fig. 4.11l).

During December, height anomalies with opposite signs alternate from the northwestern Pacific to Greenland in the lower stratosphere

(shading in Fig. 4.11f). This pattern is similar to the pattern of anomalous tropopause pressure anomalies in December (Fig. 4.2b). In particular, negative height anomaly over Greenland becomes stronger from mid-December, and poleward momentum flux develops strongly in the North Atlantic region (figure not shown). This momentum flux, which is related to strong equatorward EP flux anomalies in late December–early January (shading in Fig. 4.8d), may be linked to a reduction in upward EP flux toward the stratospheric polar vortex (Figs. 4.7h).

From mid-February, positive height anomaly and easterly wind anomaly begin to develop in the Arctic stratosphere (Figs. 4.7g and 4.11c–e). The anomalous easterly is related to an increase in upward EP flux associated with the tropospheric high anomalies in the North Atlantic and Ural region and the tropospheric low anomaly in the northwestern Pacific during the phase transition period (shading in Fig. 4.11m). In the lower stratosphere and troposphere, positive height anomaly develops over the Arctic from March and continues through April (shading in Fig. 4.11i, j, n, and o). In the lower troposphere, mid-latitude low anomalies are seen over Europe and the central North Pacific. The meridional gradient of height anomalies is opposite to that in the winter phase (shading in Fig. 4.11l and n). Compared with the tropospheric pattern in January, the center of action of the mid-latitude height anomalies is shifted slightly eastward (westward) in the Atlantic (Pacific) sector and the polar height anomalies are more asymmetric in the zonal direction.

The perturbed vortex in the second mode shows a development in

which its center moves toward the pole as the vortex strengthens in December–January (green dashed contour in Fig. 4.11a and b), and then moves to the northern Europe as it weakens in March (Fig. 4.11d). The strong stratospheric anomalies in March can exert a strong influence on the fragile spring vortex, much greater than the impact of winter anomalies on the strong winter vortex (Fig. 4.11b and d).

This section shows that the center of stratospheric vortex shifts toward the northern Europe as it weakens and its center moves closer to the pole as it strengthens. This is true for both the modes even though the evolution patterns are different. In the lower troposphere, AO/NAO-like pattern appears in both modes. Mid-latitude anomalies, however, exhibit significant zonal asymmetry and do not evolve in the same manner as the high-latitude anomalies. These regional variations will be discussed further in the next sections in terms of tropospheric jet fluctuations in the Atlantic and Pacific regions.

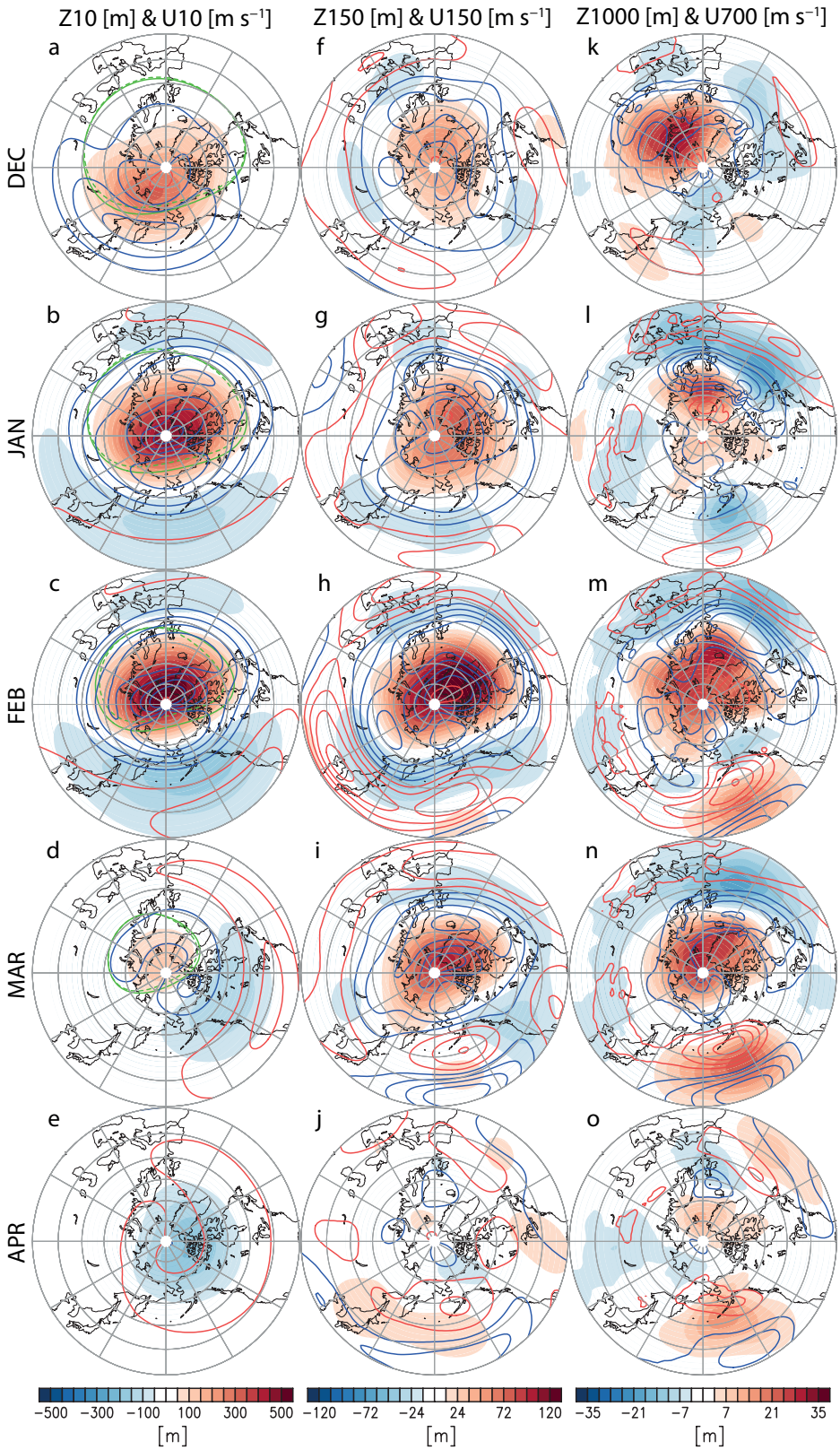
Z10 [m] & U10 [m s⁻¹]
Z150 [m] & U150 [m s⁻¹]
Z1000 [m] & U700 [m s⁻¹]
DEC
JAN
FEB
MAR
APR
a
b
c
d
e
f
g
h
i
j
k
l
m
n
o
−500 −300 −100 100 300 500
[m]
−120 −72 −24 24 72 120
[m]
−35 −21 −7 7 21 35
[m]

Figure 4.10. Monthly mean patterns of (a–e) 10-hPa geopotential height anomalies [shading, m] and 10-hPa zonal wind anomalies [red (+) and blue (–) contours at ±3, 6, 9, and 12 m s^{-1}] with the seasonal cycle of climatological geopotential height (green solid contour at 30170 m) and perturbed geopotential height (green dashed contour at 30170 m), (f–j) 150-hPa geopotential height anomalies [shading, m] and 150-hPa zonal wind anomalies [red (+) and blue (–) contours at ±0.5, 1.5, 2.5, and 3.5 m s^{-1}], and (k–o) 1000-hPa geopotential height anomalies [shading, m] and 700-hPa zonal wind anomalies [red (+) and blue (–) contours at ±0.5, 1, 1.5, and 2 m s^{-1}] for the first CSEOF mode. The perturbed geopotential height is obtained by adding the climatology with a 1σ value of the anomalous geopotential height. 30170 m contour is considered as a polar vortex boundary, which corresponds to geopotential height contour at climatological zonal wind maximum location.

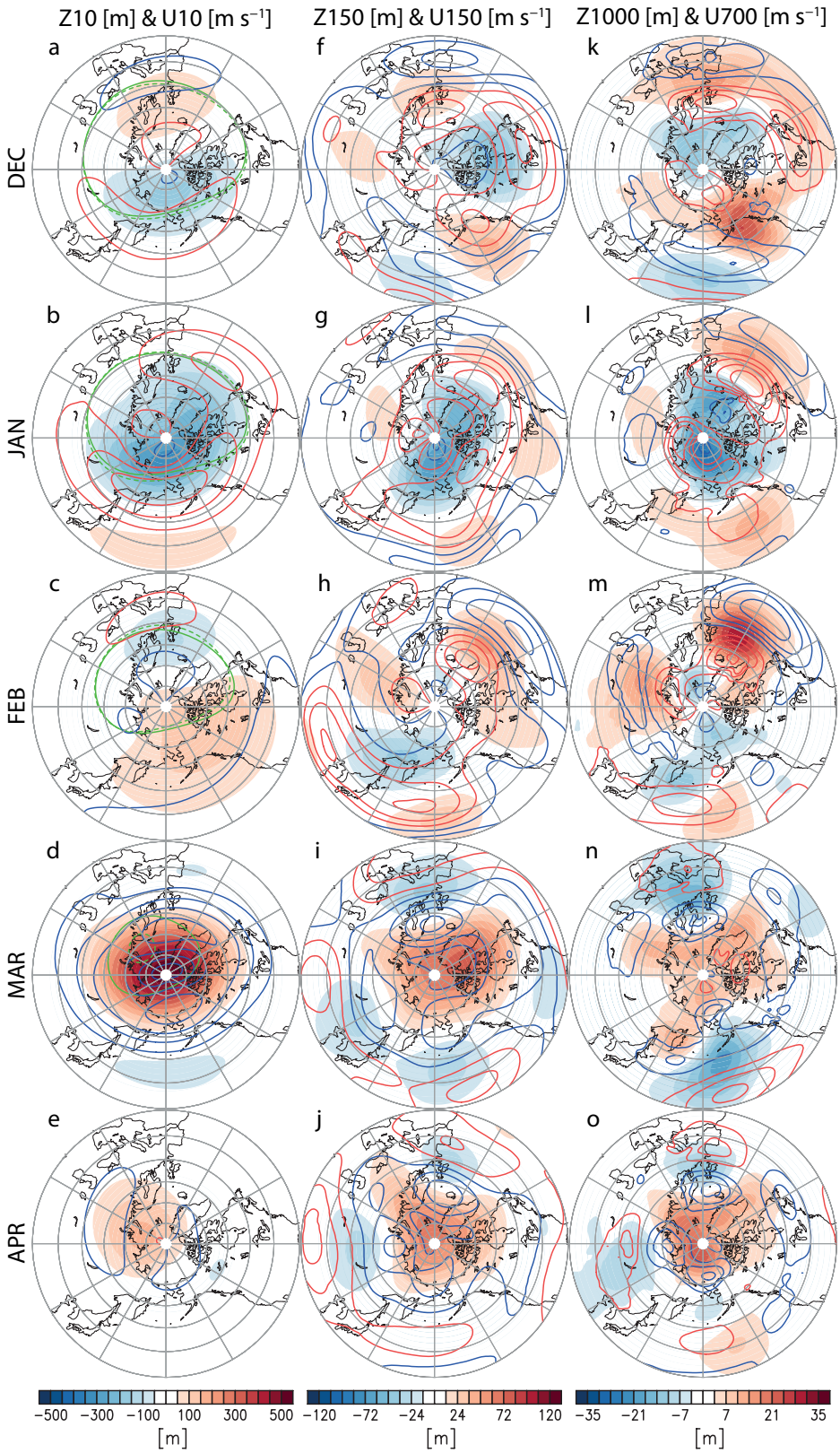
Z10 [m] & U10 [m s⁻¹]
Z150 [m] & U150 [m s⁻¹]
Z1000 [m] & U700 [m s⁻¹]
DEC
JAN
FEB
MAR
APR
a
b
c
d
e
f
g
h
i
j
k
l
m
n
o
−500 −300 −100 100 300 500
[m]
−120 −72 −24 24 72 120
[m]
−35 −21 −7 7 21 35
[m]

Figure 4.11. Monthly mean patterns of (a–e) 10-hPa geopotential height anomalies [shading, m] and 10-hPa zonal wind anomalies [red (+) and blue (–) contours at ±3, 6, 9, and 12 m s^{-1}] with the seasonal cycle of climatological geopotential height (green solid contour at 30170 m) and perturbed geopotential height (green dashed contour at 30170 m), (f–j) 150-hPa geopotential height anomalies [shading, m] and 150-hPa zonal wind anomalies [red (+) and blue (–) contours at ±0.5, 1.5, 2.5, and 3.5 m s^{-1}], and (k–o) 1000-hPa geopotential height anomalies [shading, m] and 700-hPa zonal wind anomalies [red (+) and blue (–) contours at ±0.5, 1, 1.5, and 2 m s^{-1}] for the second CSEOF mode. The perturbed geopotential height is obtained by adding the climatology with a 1σ value of the anomalous geopotential height. 30170 m contour is considered as a polar vortex boundary, which corresponds to geopotential height contour at climatological zonal wind maximum location.

4.4. Mid-latitude tropospheric jet fluctuation and its linkage to the tropopause undulation

The temporally varying centers of action in mid-latitude circulation anomalies cause regional differences in the response of the tropospheric jets. Tropospheric jets behave differently in the Atlantic and Pacific regions, indicating regionally asymmetric stratosphere-troposphere coupling. This is clearly seen in the first mode (Fig. 4.12a–f). The easterly anomaly decelerates the poleward side and the mid-latitude westerly anomaly accelerates the equatorward side of the Atlantic jet (shading in Fig. 4.12a–c). The Atlantic jet axis moves equatorward, which is frequently accompanied by the weakening of stratospheric polar vortex (Kidston et al. 2015). The polar easterly anomaly is located further north in the Pacific region and barely affects the Pacific jet (Fig. 4.12d–f). The weakened impact of stratospheric polar jet deceleration on the Pacific jet is due to the large meridional separation, and is similar to the result of Davini et al. (2014). In January, the tropospheric Pacific jet is strengthened by the mid-latitude westerly anomaly (Fig. 4.12d). In February and March, the axis of the Pacific jet migrates poleward (circle symbols in Fig. 4.12e and f), which is the opposite to the jet movement in the Atlantic (Fig. 4.12b and c).

The mid-latitude tropopause anomalies are much weaker and smaller, which nonetheless reflect the tropospheric jet variations. The anomalous tropopause pressure gradient is, in general, positively correlated with the tropospheric zonal wind variation near the jet stream (Fig. 4.13). This, from

the PV perspective, is because positive (negative) tropopause pressure anomalies are dynamically balanced with cyclonic (anticyclonic) anomalies at the UTLS region (Seidel and Randel 2006; Zängl and Wirth 2002). In this regard, the tropospheric cyclonic anomaly in the Atlantic region coexists with the positive tropopause pressure anomaly in the first mode (Figs. 4.1c–e and 4.12a–c). In the Pacific region, the tropospheric anticyclonic anomaly coexists with the negative tropopause pressure anomaly (Figs. 4.1c–e and 4.12d–f).

This relationship is relatively clear in the mid-latitude tropopause, which contrasts with the high latitude tropopause where strong coupling with stratospheric vortex fluctuations results in decorrelation with tropospheric height variations (Fig. 4.6). It can be said, therefore, that the mid-latitude tropopause anomalies are more closely linked to tropospheric wind anomalies than the Arctic tropopause anomalies. This relationship with the tropospheric jet also appears in the zonal mean sense, which explains the wavy deformation of tropopause anomalies to the north and south of the zonal wind anomalies through meridional flux of quasigeostrophic PV at the tropopause level (Barroso and Zurita-Gotor 2016).

Unlike the first mode, where the latitude of the stratospheric polar jet anomaly differs in the Pacific and Atlantic sectors, both polar jet anomalies develop around 60°N in the second mode (shading in Fig. 4.12g–l). In January, intensification of the stratospheric polar vortex is manifested as an acceleration on the polar side of the Atlantic and Pacific jets (Fig. 4.12g and j). The Atlantic jet migrates poleward, but the Pacific jet shows no latitudinal shift in its axis and slows down slightly. In February, when the stratospheric

vortex fluctuation begins to weaken, a poleward migration of the Atlantic jet, along with deceleration, is seen in the mid-lower troposphere (Fig. 4.12h). At this time, the Pacific jet speeds up (Fig. 4.12k). Weakening of the stratospheric vortex in March is connected with the weakening of the Atlantic jet strength and deceleration on the polar side of the Pacific jet (Fig. 4.12i and l). In addition, the Pacific jet is strengthened as opposed to January. The associated mid-latitude tropopause anomalies and their gradient are more complicated than the first mode, particularly in the Pacific (Fig. 4.2c and).

The steeper tropopause slope in the jet stream is also related to the increase in the tropopause folding frequency (figure is not shown). This is because tropopause folding occurs in regions of the strong meridional temperature gradient and vertical wind shear (Holton 2004), in association with the upper tropospheric jet strength. While tropopause folding is an important phenomenon in understanding stratosphere-troposphere mass exchange, this thesis focuses only on the dynamical coupling of stratosphere and troposphere.

In summary, tropospheric jet fluctuations are not only different in the two oceanic sectors but also vary in time despite the persistence of the stratospheric vortex fluctuation in the first mode. In the second mode, it is found that the change in the mid-latitude jets is not simply of opposite signs in January and March as in the stratospheric vortex. From a regional perspective, these results indicate that zonal asymmetry in the variation of stratospheric and tropospheric zonal winds is an important characteristic of the leading modes of tropopause variability.

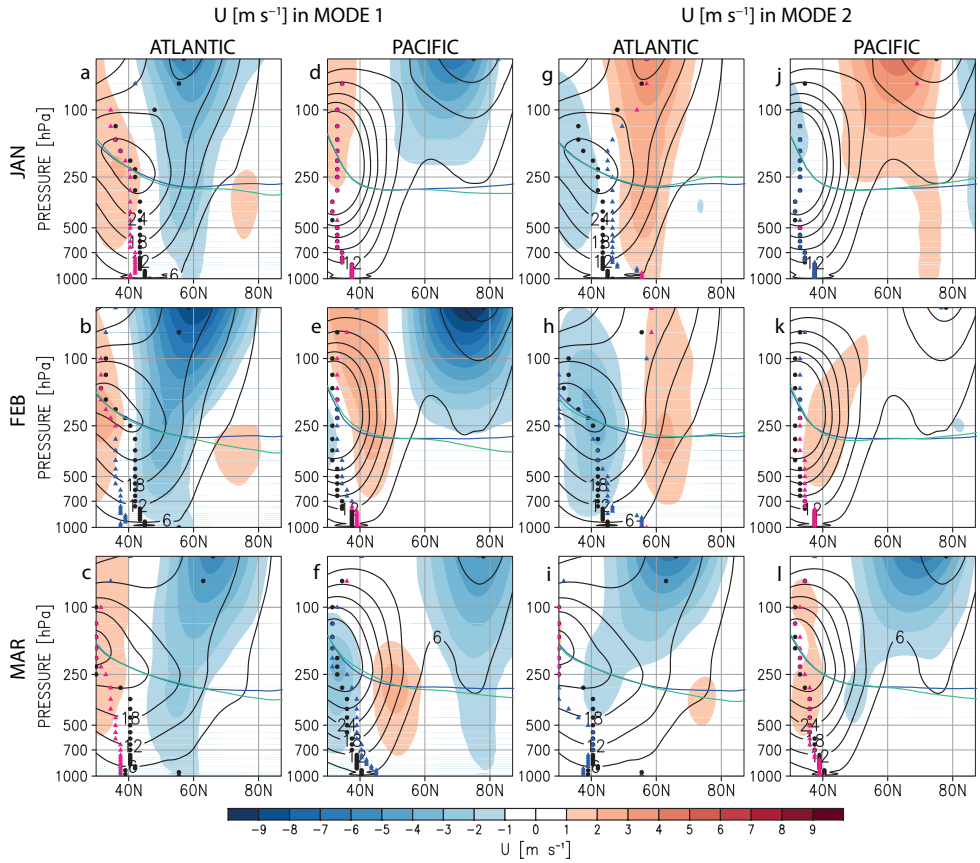

Figure 4.12. Latitude-altitude monthly mean patterns of zonal wind anomalies [m s^{-1}] (shading) and climatological zonal wind [contours at 6 m s^{-1} interval] and jet axis of the climatology (black circle) and perturbed wind (color triangle, red: acceleration, blue: deceleration) and the climatological tropopause (blue line) and perturbed tropopause (aqua line) over (a–c, g–i) the Atlantic [90°–10°W] and (d–f, j–l) the Pacific [120°–230°E] regions during the period of strong stratospheric variation in (a–f) the first and (g–l) the second CSEOF mode of tropopause variability. The perturbed field is obtained by adding the climatology with the 2σ values of the anomalous field.

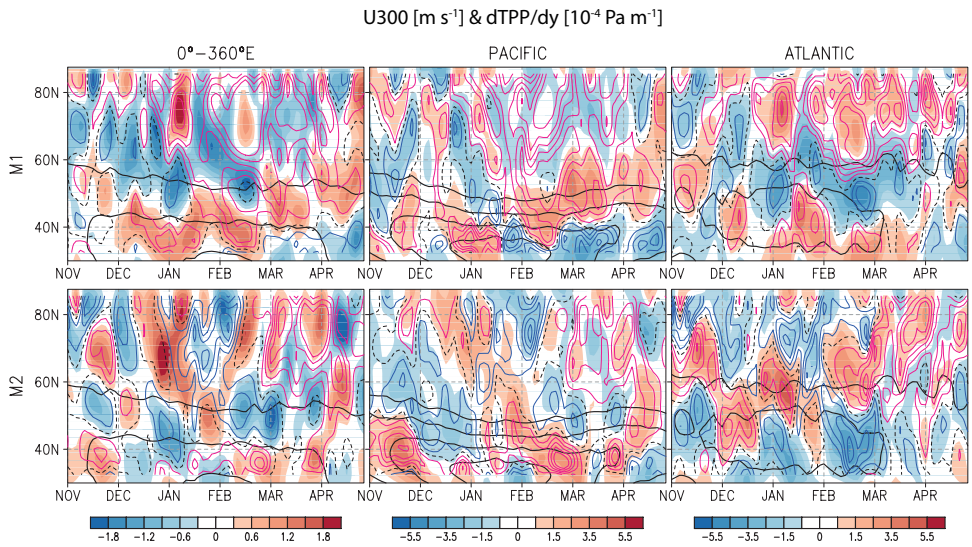

Figure 4.13. Time-latitude patterns of the 300-hPa longitudinal mean zonal wind anomalies (shading), meridional gradient of tropopause pressure anomalies (magenta (+) and blue (–) contours) and the climatological westerly jet (black contour) over (first column) the whole domain [0°–360°E], (second column) the Pacific sector [120°–230°E], and (third column) the Atlantic sector [90°–10°W] for (upper) the first and (lower) the second CSEOF modes. The dashed line represents the zero contour.

4.5. Role of the two modes in the extreme stratospheric vortex events

Reconstructed data based on the two modes accounts for more than 40 (50) % of the total variance of the PCH index at 10 (50) hPa. In addition, the reconstructed data are significantly correlated with the raw data in the stratosphere with a correlation value of ~0.65 (~0.74) at 10 (50) hPa (Figs. 4.14 and 4.15). As can be seen in Fig. 8, evolution patterns of the PCH anomalies are reasonably similar between the two, although significant differences are also seen in some years. This suggests that PCH variability in the stratosphere can be explained to some extent in terms of the two CSEOF modes. More precisely, the PCH variability can be explained to some extent by the stratospheric fluctuations that induce the Arctic tropopause fluctuations in the two modes. In the troposphere, however, the PCH variability associated with the leading modes of tropopause pressure tend to be obscured because of strong internal variability (Fig. 4.15). In this study, the normalized PCH index is used as a proxy for the Northern Annular Mode (NAM) index, which describes variation of the polar vortex strength (Baldwin and Dunkerton 2001; Baldwin and Thompson 2009). If a local extremum of the 10-hPa NAM index is greater than $+1.5\sigma$, a weak vortex event is assumed to have occurred, and a strong vortex event is assumed to have occurred if it is less than -1.5σ. Thresholds are generally set to ±1–3σ (Baldwind and Dunkerton 2001; Limpasuvan 2004; 2005), and in this study, the same threshold as in Runde et al. (2016) is used. The minimum distance between two adjacent events is set

to 12 pentads (2 months) based on the peak date of each event; any two events not separated by the minimum distance are considered as a single event and the larger of the two peaks is chosen as the strength of the extreme event. For composite analysis, the strongest event in each polarity for a given year is used.

The tropopause-related vertical evolution explains the long persistency of typical extreme vortex events (Fig. 4.16). The two modes contribute to the gradual decline of weak vortex (WV) events in the stratosphere (Fig. 4.16a–f); without the two modes a weak vortex event will in general end quickly (within a month). The two modes are also strongly responsible for the intensity and the persistence of strong vortex (SV) events in the stratosphere (Fig. 4.16g–l). However, it seems that contribution from other CSEOF modes is additionally needed to fully explain the asymmetry between the positive and negative events in other studies (Huang 2017; Limpasuvan et al. 2005; Martineau and Son 2010).

In addition to the composite characteristics of extreme vortex events, it should also be noted that their evolution characteristics and the timing of occurrence vary significantly from one case to another. The two modes not only explain the total PCH variation to some extent as mentioned above, but also explain reasonably the intraseasonal evolution of stratospheric vortex each year. The irregular interplay of the two modes with distinctive evolutionary characteristics is expected to produce the diversity of vortex events. Therefore, it is necessary to distinguish the contributions of the two modes in order to understand how they shape the individual characteristics of

vortex events.

Figure 4.17 depicts the amplitudes of the first and the second modes for each vortex event, and shows fairly uneven contributions of the two modes. This figure shows only the cases when the 10-hPa PCH index of the two-mode reconstruction has the same polarity as the event on the peak date. Since the two modes of the tropopause pressure are characterized by low-frequency modulation, their superposition is insufficient to form a rapid vortex event shorter than 2 months and more than two events a year. If the amplitude of any of the two modes is greater than +1 or less than −1, it is considered to make an active contribution to the occurrence of the pertaining event (color symbols in Fig. 4.17). There are more WV events in the positive phase and more SV events in the negative phase of the first mode (Fig. 4.17). This indicates that WV and SV events tend to develop preferably when the first mode is in a positive and negative phase, respectively. The phase of the second mode seems to be involved in the timing of extreme events between winter and spring. WV events in February–March are generally associated with the positive phase of the second mode, and events in January are associated with the negative phase. SV events in January–February mostly accompany the positive phase of the second mode, and events in March–April accompany the negative phase. In the same context, if both WV and SV events occur in a given year, the sequence of events is related to the phase of the second mode. In particular, when the second mode is in a positive phase, events tend to occur in the order of winter SV and spring WV (more cross symbols in the positive phase of the second mode).

To summarize, tropopause related stratosphere-troposphere variation explains the long persistence of typical extreme vortex events. For the interannual variation of extreme vortex events, the first mode is associated with the polarity of the event, and the second mode contributes to determining the approximate timing of the event. Actual extreme vortex events occur on more diverse time scales. Nevertheless, the fact that the timing of events depends on the strength of each mode indicates that the leading two modes serve as a rough guideline for determining evolutionary structures of extreme events (Figs. 4.15 and 4.17).

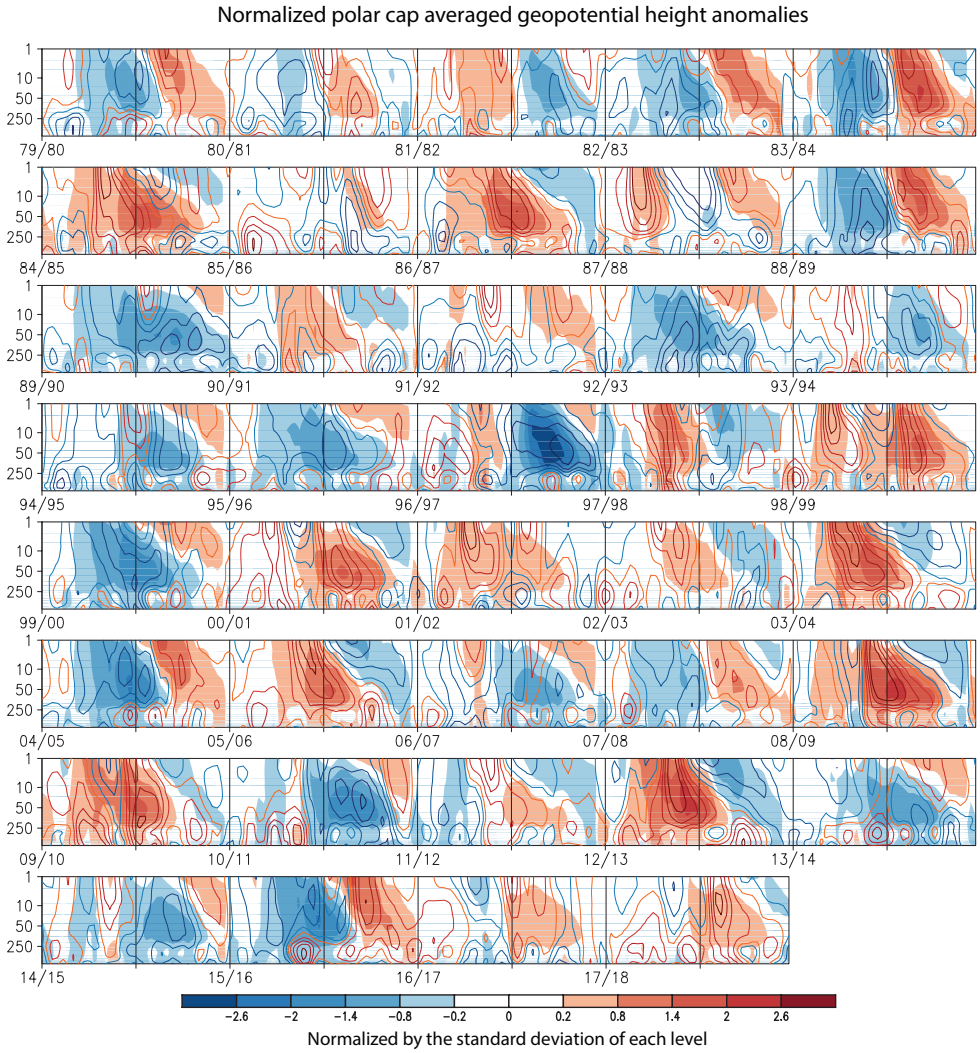

Figure 4.14. Normalized polar cap averaged [0°–360°E, 65°–87°N] geopotential height (PCH) anomalies from the reconstructed data based on the first two CSEOF modes of tropopause variability (shaded) and that from the raw data (contour) during the data period (1979–2018).

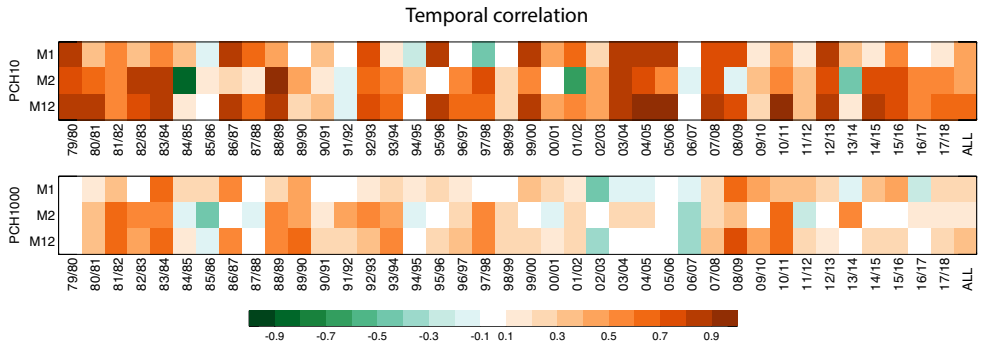

Figure 4.15. Temporal correlation between the raw data and reconstructed data based on the first two CSEOF modes for each year: (upper) 10-hPa and (lower) 1000-hPa PCH anomalies.

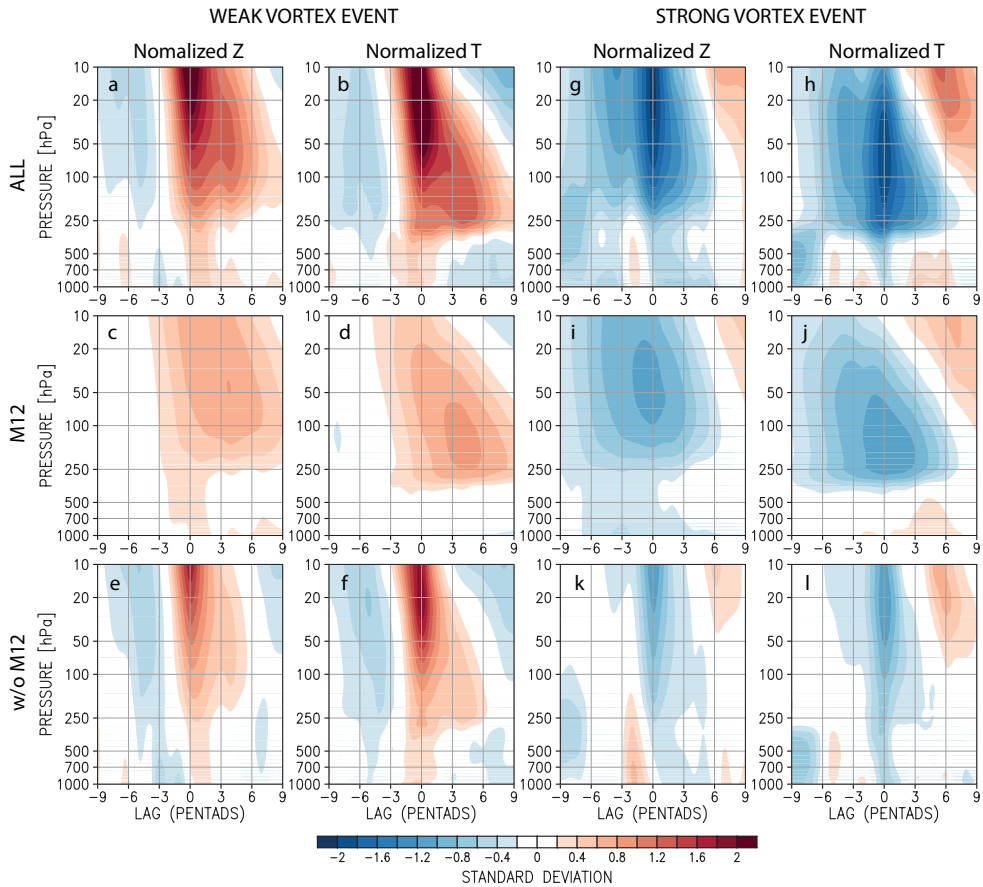

Figure 4.16. Composite time-altitude patterns of the normalized polar-cap averaged [0°–360°E, 65°–87°] (the first and third columns) geopotential height anomalies and (the second and fourth columns) temperature anomalies for (a–f) the weak events and (g–l) the strong events of the stratospheric polar vortex. The first row represents the raw data, the second row is based on the first two CSEOF modes, and the third row represents the raw data without the first two CSEOF modes. The 10-hPa polar cap height (PCH) index greater (less) than $+1.5\sigma$ (-1.5σ) is defined as the weak (strong) vortex events. For composite patterns, the strongest event of each polarity in a given year is used. The abscissa denotes lag in pentads with respect to the timing of the strongest event.

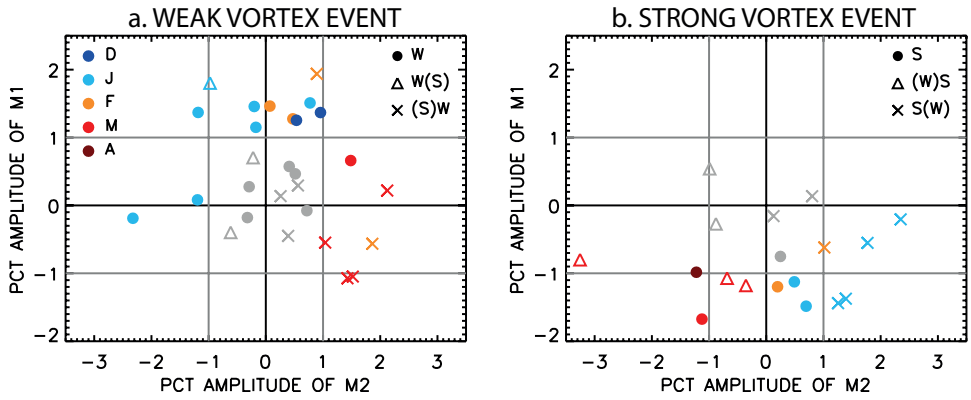

Figure 4.17. PC time series amplitude of the first (y axis) and the second (x axis) modes of tropopause variability for (a) the 28 weak and (b) the 18 strong events of the stratospheric polar vortex. Events are grouped according to the following criteria: active/inactive contribution of the modes to weak/strong vortex events (color/grey symbols), occurrence of a single event in a given year (circle), and occurrence of events with both polarities in a given year (triangle: weak vortex followed by strong vortex; cross: strong vortex followed by weak vortex).

Chapter 5. Concluding remarks

In the first part of this thesis (chapter 3), we have examined the leading modes of Arctic SIC variability for 39 winters and delineated corresponding changes in stratospheric polar vortex. The first mode represents an accelerating trend of Arctic sea ice decline associated with Arctic amplification, particularly in the Barents and Kara Seas. A rapid sea ice reduction in the Arctic around the BKS is related to a stratospheric polar vortex weakening in mid-January–late February. The second mode exhibits a dipole structure of sea ice variation with an out-of-phase relationship between the eastern and western North Atlantic associated with NAO circulation. The dipole pattern corresponding to negative NAO-like circulation, the anomalous increase of SIC in the Barents and Greenland Seas and the anomalous decrease in the Labrador Sea and Hudson Bay, in the second mode is accompanied by a stratospheric vortex weakening in December–early February. In addition, the stratospheric polar vortex weakening is different in geometric features between the two modes. In the mature phase of stratospheric anomalies, stratospheric vortex migrates to Eurasia in the first mode and to Europe in the second mode.

It should be noted that stratospheric vortex weakening over the Barents Sea is related to the SIC reduction in the first mode and the SIC augmentation in the second mode. Several studies suggested that geographical location of SIC loss is an important factor in determining stratospheric response (Mckenna et al. 2018; Screen 2017a; Sun et al. 2015).

Our result, on the other hand, indicates that stratospheric vortex variation depends on the overall pattern of SIC loss in the entire Arctic. Not only the timing of stratospheric vortex weakening, but also movement or deformation of vortex depend critically on the modal pattern of SIC reduction. In order to better understand SIC-related stratospheric vortex variation, therefore, it seems necessary to first identify the mode of SIC variability.

It is expected that stratospheric vortex weakening will occur frequently during mid-January to late February as SIC reduction accelerates. In addition, it can be predicted that in the mature stage the upper stratospheric vortex will move toward Eurasia. On the other hand, the amplitude of the Atlantic dipole SIC variations, which shows a transition toward a positive phase during the 1980–2000s, has been small in recent years. Accordingly, the December–January weakening of stratospheric vortex, which tends to migrate toward Europe in the mature stage, had intensified until the 2000s and then has recently subsided. The results suggest that the two SIC modes partly have contributed to a long-term change in subseasonal evolution of stratospheric vortex.

The stratospheric vortex fluctuations associated with the two leading SIC modes account for approximately 6% (14%) of the total variance of 10 hPa (100 hPa) PCH index. This implies that the internal variability of stratospheric vortex away from the major SIC variability is greater than the SIC-related vortex variation. Nevertheless, this study is meaningful in that it distinguishes the distinct evolution aspects of stratospheric variations associated to the major modes of SIC variability arising from forced climate

change and natural variability.

In the second part of this thesis, the leading modes of NH tropopause pressure variability for November–April of 1979–2018 and the associated physical variations in the stratosphere and the troposphere were analyzed. The first two modes, marked by anomalous tropopause pressure concentrated in the Arctic, describe connections between the stratospheric polar vortex strength and the high-latitude tropospheric circulation. Arctic tropopause pressure is directly affected by stratospheric temperature fluctuations. Stratospheric warming associated with stratospheric polar vortex weakening increases the Arctic tropopause pressure. The first mode reflects a stratospheric polar vortex disturbance lasting from winter to early spring. The second mode represents weak polar vortex fluctuations in winter followed by strong spring vortex fluctuations of opposite polarity.

An examination of the zonally asymmetrical component of the two modes reveals that stratospheric polar vortex weakening is linked to equatorward migration of the Atlantic jet axis and poleward migration of the Pacific jet axis in the first mode. This means that the coupling between the stratospheric polar jet and tropospheric mid-latitude jet is different in the two regions. The regional difference in the zonal wind anomalies is reflected in the mid-latitude tropopause fluctuations in terms of the PV inversion relation, which is particularly apparent in the first mode. This behavior corresponds to a tropopause pressure increase in the Atlantic and a decrease in the Pacific. For the second mode, the Atlantic jet axis moves poleward in winter, but in spring the maximum speed of the Atlantic jet only weakens without axis

movement. During this period, the maximum wind speed decreases in winter and the maximum wind speed increases in spring for the Pacific jet. Compared to the first mode, however, the associated mid-latitude tropopause anomalies are much weaker and more complex.

It should be noted that the two types of stratosphere-troposphere evolution can provide deeper insight into distinct evolution properties of extreme vortex events. The phase of the first mode essentially controls the polarity of extreme events, and the phase of the second mode is strongly tied with the timing of extreme events. As a result, the superposition of physically and statistically distinct modes of tropopause variability can help understand the evolution of individual NAM events and their potential timing of occurrence, thereby improving the seasonal predictability of the Arctic climate during the cold season. This means that the leading modes of the tropopause variability can be a useful tool for understanding the slowly evolving intraseasonal interaction between the stratosphere and troposphere.

In summary, the first part provides a better understanding of the historical changes in sea ice-stratospheric vortex linkage by delineating distinct evolutions of stratospheric vortex for two different sea ice modes. In the second part, intrinsic evolutionary features of stratosphere-troposphere variations in terms of tropopause modes are identified, providing a deeper understanding of stratosphere-troposphere coupling, including the diversity of vortex events.

References

Ambaum MH, Hoskins BJ (2002) The NAO Troposphere-Stratosphere Connection. J Clim 15:1969:1978

Baldwin MP, Dunkerton TJ (2001) Stratospheric Harbingers of Anomalous Weather Regimes. Science 294:581-584

Baldwin MP, Thompson DWJ (2009) A critical comparison of stratosphere-troposphere coupling indices. Q J Royal Meteorol Soc 135:1661-1672

Baldwin MP, Birner T, Brasseur G, Burrows J, Butchart N, Garcia R, Geller M, Gray L, Kevin Hamlington, Harnik N, Hegglin MI, Langematz U, Robock A, Sato K, Scaife AA (2019) 100 Years of Progress in Understanding the Stratosphere and Mesosphere. Meteor Monogr 59:27.1–27.62. https://doi.org/10.1175/AMSMONOGRAPHS-D-19-0003.1

Baldwin MP et al. (2021) Sudden Stratospheric Warmings. Reviews of Geophysics 59: e2020RG000708. doi.:10.1029/2020RG000708

Barroso JA, Zurita-Gotor P (2016) Intraseasonal Variability of the Zonal-Mean Extratropical Tropopause: The Role of Changes in Polar Vortex Strength and Upper-Troposphere Wave Breaking. J Atmos Sci 73:1383-1399

Blackport R, Screen JA, van der Wiel K, Richard B (2019) Minimal influence of reduced Arctic sea ice on coincident cold winters in mid-latitudes. Nat Clim Change 9:697-704. https://doi.org/10.1038/s41558-019-0551-4

Cai M, Ren R-C (2007) Meridional and Downward Propagation of Atmospheric Circulation Anomalies. Part I: Northern Hemisphere Cold Season Variability. J Atmos Sci 64:1880–1901. https://doi.org/10.1175/JAS3922.1

Charlton AJ, Polvani LM (2007) A New Look at Stratospheric Sudden Warmings. Part I: Climatology and Modeling Benchmarks. J Clim 20:449–469. https://doi.org/ 10.1175/JCLI3996.1

Chen X, Luo D (2017) Arctic sea ice decline and continental cold anomalies: Upstream and downstream effects of Greenland blocking. Geophys Res Lett 44(7):3411–3419. https://doi.org/ 10.1002/2016GL072387

Cohen J, Pfeiffer K, Francis JA (2018) Warm Arctic episodes linked with increase frequency of extreme winter weather in the United States. Nat Commun 9:869. https://doi.org/10.1038/s41467-018-02992-9

Cohen J, Screen JA, Furtado JC et al (2014) Recent Arctic amplification and extreme mid-latitude weather. Nat Geosci 7:627-637

Cohen J, Zhang X, Francis J et al (2020) Divergent consensuses on Arctic amplification influence on midlatitude severe winter weather. Nature Climate Change 10:20–29. https://doi.org/10.1038/s41558-019-0662-y

Davini P, Cagnazzo C, Anstey JA (2014) A blocking view of the stratosphere-troposphere coupling. J Geophys Res Atmos 119:1100-1115. https://doi.org/10.1002/2014JD021703

Dee DP, Uppala SM, Simmons AJ et al (2011) The ERA-interim reanalysis: configuration and performance of the data assimilation system. Q J Royal Meteorol Soc 137:553-597

Deser C, Teng H (2008) Evolution of Arctic sea ice concentration trends and the role of atmospheric circulation forcing, 1979—2007. Geophys Res Lett 35:L020504. https://doi.org/10.1029/2007GL032023

Deser C, Walsh JE, Timlin MS (2000) Arctic Sea Ice Variability in the Context of Recent Atmospheric Circulation Trends. J Clim 13:617-633

Garfinkel CI, Hartmann DL (2008) Different ENSO teleconnections and their effects on the stratospheric polar vortex. J Geophys Res 113: D18114. https://doi.org/10.1029/2008JD009920

Garfinkel CI, Benedict JJ, Maloney ED (2014) Impact of the MJO on the boreal winter extratropical circulation. Geophys Res Lett 41:6055–6062. https://doi.org/10.1002/2014GL061094

Garfinkel CI, Hartmann DL, Sassi F (2010) Tropospheric Precursors of Anomalous Northern Hemisphere Stratospheric Polar vortices. J Clim 23:3282-3299

Gerber EP, Orbe C, Polvani LP (2009) Stratospheric influence on the tropospheric circulation revealed by idealized ensemble forecasts.

Geophys Res Lett 36:L24801. https://doi.org/10.1029/2009GL040913

Hassanzadeh P, Kuang Z (2015) Blocking variability: Arctic Amplification versus Arctic Oscillation. Geophys Res Lett 42:8586–8595. Https://doi.org/10.1002/2015GL065923

Hitchcock P, Simpson IR (2014) The Downward Influence of Stratospheric Sudden Warmings. J Atmos Sci 71:3856–3876. https://doi.org/10.1175/JAS-D-14-0012.1

Hitchcock P, Shepherd TG, Manney GL (2013) Statistical characterization of Arctic polar-night jet oscillation events. J Clim 26:2096–2116. https://doi.org/ 10.1175/JCLI-D-12-00202.1

Honda M, Inoue J, Yamane S (2009) Influence of low Arctic sea-ice minima on anomalously cold Eurasian winters. Geophys Res Lett 36:L08707. https://doi.org/10.1029/2008GL037079

Hoshi K, Ukita J, Honda M, Iwamoto K, Nakamura T, Yamazaki K, Dethloff K, Jaiser R, Handorf D (2017) Poleward eddy heat flux anomalies associated with recent Arctic sea ice loss. Geophys Res Lett 44:446–454. https://doi.org/10.1002/2016GL071893

Hoshi K, Ukita J, Honda M, Nakamura T, Yamazaki K, Miyoshi Y, Jaiser R (2019) Weak Stratospheric Polar Vortex Events Modulated by the Arctic Sea-Ice Loss. J Geophys Res Atmos 124:858–869. https://doi.org/10.1029/2018JD029222

Hu A, Rooth C, Bleck R, Deser C (2002) NAO influence on sea ice extent in the Eurasian coastal region. Geophys Res Lett 29:2053. https://doi.org//10.1029/2001GL014293

Huang J, Tian W, Gray LJ, Zhang J, Li Y, Luo J, Tian H (2018) Preconditioning of Arctic Stratospheric Polar Vortex Shift Events. J Clim 31:5417–5436. https://doi.org/10.1175/JCLI-D-17-0695.1

Jaiser R, Nakamura T, Handorf D, Dethloff K, Ukita J, Yamazaki K (2016) Atmospheric winter response to Arctic sea ice changes in reanalysis data and model simulations. J Geophys Res Atmos 121:7564–7577.

https://doi.org/10.1002/2015JD024679

Jucker M (2016) Are Sudden Stratospheric Warming Generic? Insights from an Idealized GCM. J Atmo Sci 73:5061–5080

Kidston J, Scaife AA, Hardiman SC, Mitchell DM, Butchart N, Baldwin MP, Gray LJ (2015) Stratospheric influence on tropospheric jet streams, storm tracks and surface weather. Nat Geosci 8:433–440. https://doi.org/10.1038/NGEO2424

Kim KY (2017) Cyclostationary EOF Analysis: Theory and Applications. SNU press, 446pp

Kim KY, Hamlington BD, Na H (2015) Theoretical foundation of cyclostationary EOF analysis for geophysical and climatic variables: concepts and examples. Earth-Sci Rev 150:201-218

Kim KY, Hamglington BD, Na H, Kim J (2016) Mechanism of seasonal Arctic sea ice evolution and Arctic amplification. Cryosphere 10:2191–2202. https://doi.org/10.5194/tc-10-2191-2016

Kim KY, Kim J, Kim J, Yeo S, Na H, Hamlington BD, Leben RR (2019) Vertical Feedback Mechanism of Winter Arctic Amplification and Sea Ice Loss. Sci Rep 9:1184. https://doi.org/10.1038/s41598-018-38109-x

Kim KY, North GR (1997) EOFs of harmonizable cyclostationary processes. J Atmospheric Sci 54:2416–2427

Kim KY, North GR, Huang J (1996) EOFs of one-dimensional cyclostationary time series: computations, examples, and stochastic modeling. J Atmospheric Sci 53:1007–1017

Kim KY, Son SW (2016) Physical characteristics of Eurasian winter temperature variability. Environ Res Lett 11:044009. https://doi.org/10.1088/1748-9326/11/4/044009

Kim BM, Son SW, Min SK, Jeong JH, Kim SJ, Zhang X, Shim T, Yoon JH (2014) Weakening of the stratospheric polar vortex by Arctic sea-ice loss. Nat Commun 5:4646. https://doi.org/10.1038/ncomms5646

Lawrence ZD, Manney GL (2018) Characterizing stratospheric polar vortex variability with computer vision techniques. J Geophys Res Atmos

123:1510–1535. https://doi.org/10.1002/2017JD027556

Limpasuvan V, Hartmann DL (2000) Wave-Maintained Annular Modes of Climate Variability. J Clim 13(24):4414–4429. https://doi.org/10.1175/1520-0442(2000)013<4414:WMAMOC>2.0.CO;2

Limpasuvan V, Thompson DWJ, Hartmann DL (2004): The life cycle of the Northern Hemisphere sudden stratosphere warmings. J Clim 17:2584–2596

Limpasuvan V, Hartmann DL, Thompson DWJ, Kumar Jeev, Yung YL (2005) Stratosphere-troposphere evolution during polar vortex intensification. J Geopys Res 110:D24101. https://doi.org/10.1029/2005JD006302

Lorenz DJ, DeWeaver ET (2007) Tropopause height and zonal wind response to global warming in the IPCC scenario integrations. 112:D10119. https://doi.org/10.1029/2006JD008087

Luo D, Xiao Y, Yao Y et al. (2016) Impact of Ural Blocking on Winter Warm Arctic–Cold Eurasian Anomalies. Part I: Blocking-Induced Amplification. J Clim 29:3925–3947. https://doi.org/ 10.1175/JCLI-D-15-0611.1

Magnusdottir G, Deser C, Saravanan R (2004) The effects of North Atlantic SST and sea ice anoamlies on the winter circulation in CCM3. Part I: main features and storm track characteristics of the response. J Clim 17:857–876

Martineau P and Son SW (2010) Quality of reanalysis data during stratospheric vortex weakening and intensification events. Geophys Res Lett 37:L22801. https://doi.org/10.1029/2010GL045237

Martius O, Polvani LM, Davies HC (2009) Blocking precursors to stratospheric sudden warming events. Geophys Res Lett 36(14):L14806. https://doi.org/10.1029/2009GL038776

Maycock AC, Hitchcock (2015) Do split and displacement sudden stratospheric warmings have different annular mode signatures?

Geophys Res Lett 42:10943–10951. https://doi.org/10.1002/2015GL066754

McKenna CM, Bracegirdle TJ, Shuckburgh EF, Haynes PH, Joshi MM (2018) Arctic Sea Ice Loss in Different Regions Leads to Contrasting Northern Hemisphere Impacts. Geophys Res Lett 45:945–954. https://doi.org/10.1002/2017GL076433

Mitchell DM, Gray LJ, Anstey J, Baldwin MP, Charlton-Perez AJ (2013) The influence of stratospheric vortex displacements and splits on surface climate. J Clim 26:2668–2682

Mori M, Watanabe M, Shiogama H, Inoue J, Kimoto M (2014) Robust Arctic sea-ice influence on the frequent Eurasian cold winters in past decades. Nat Geosci 7:869–873. https://doi.org/10.1038/ngeo2277

Nakamura T, Yamazaki K, Iwamoto K, Honda M, Miyoshi Y, Ogawa Y, Tomikawa Y, Ukita J (2016) The stratospheric pathway for Arctic impacts on midlatitude climate. Geophys Res Lett 43:3494–3501. https://doi.org/10.1002/2016GL068330

Nakamura T, Yamazaki K, Iwamoto K, Honda M, Miyoshi Y, Ogawa Y, Ukita J (2015) A negative phase shift of the winter AO/NAO due to the recent Arctic sea-ice reduction in late autumn. J Geophys Res Atmos 120:3209–3227. https://doi.org/10.1002/2014JD022848

Nishii K, Nakamura H, Miyasaka (2009) Modulations in the planetary wave field induced by upward-propagating Rossby wave packets prior to stratospheric sudden warming events: A case-study. Q J Royal Meteorol Soc, 135:39–52

Overland JE, Wood KR, Wang M (2011) Warm Arctic-cold continents: climate impacts of the newly open Arctic Sea. Polar Res 30:15787. https://doi.org/10.3402/polar.v30i0.15787

Peings Y (2019) Ural Blocking as a Driver of Early-Winter Stratospheric Warming. Geophys Res Lett 46:5460–5468. https://doi.org/10.1029/2019GL082097

Polvani LM, Waugh DW (2004) Upward wave activity flux as a precursor to

extreme stratospheric events and subsequent anomalous surface weather regimes. J Climate 17:3548–3554

Reichler T, Dmeris M, Sausen R (2013) Determining the tropopause height from gridded data. Geophys Res Lett 30(20):2042. https://doi.org/10.1029/2003GL018240

Runde T, Dameris M, Garny H, Kinnison DE (2016) Classification of stratospheric extreme events according to their downward propagation to the troposphere. Geophys Res Lett 43:6665–6672. Https://doi.org/10.1002/2016GL069569

Screen JA (2017a) Simulated Atmospheric Response to Regional and Pan-Arctic Sea Ice Loss. J Clim 30:3945–3962

Screen JA (2017b) The missing Northern European winter cooling response to Arctic sea ice loss. Nat Commun 8:14603. https://doi.org/10.1038/ncomms14603

Screen JA, Simmonds I (2010) Increasing fall-winter energy loss from the Arctic Ocean and its role in Arctic temperature amplification. Geophys Res Lett 37:L16707. https://doi.org/10.1029/2010GL044136

Seidel D, Randel W (2006) Variability and trends in the global tropopause estimated from raidosonde data. J Geophys Res 111:D21101. https://doi.org/10.1029/2006JD007363

Seo KH, Kim KY (2003) Propagation and initiation mechanisms of the Madden-Julian oscillation. J Geophys Res 108:4384 https://doi.org/10.1029 /2002JD002876

Serreze MC, Barrett AP, Stroeve JC, Kindig DN, Holland MH (2009) The emergence of surface-based Arctic amplification. Cryosphere 3:11–19

Serreze MC, Holland MM, Stroeve J (2007) Perspectives on the Arctic's shrinking sea-ice cover. Science 315:1533–1536

Seviour WJM, Mitchell DM, Gray LJ (2013) A practical method to identify displaced and split stratospheric polar vortex events. Geophys Res Lett 40:5268-5273. https://doi.org/10.1002/grl.50927

Seviour WJM, Gray LJ, Mitchell DM (2016) Stratospheric polar vortex splits

and displacements in the high-top CMIP5 climate models. J Geophys Res Atmos 121:1400–1413. https://doi.org/10.1002/2015JD024178

Simpson IR, Blackburn M, Haigh JD (2009) The Role of Eddies in Driving the Tropospheric Response to Stratospheric Heating Perturbations. J Atmos Sci 66:1347–1365. https://doi.org/10.1175/2008JAS2758.1

Smith KL, Fletcher CG, Kushner PJ (2010) The Role of Linear Interference in the Annular Mode Response to Extratropical Surface Forcing. J Clim 23:6036–6050

Smith KL, Kushner PJ (2012) Linear interference and the initiation of extratropical stratosphere-troposphere interactions. J Geophys Res 117:D13107. https://doi.org/10.1029/2012JD017587

Strong C, Magnusdottir G (2010) Modeled winter sea ice variability and the North Atlantic Oscillation: a multi-century perspective. Clim Dyn 34:515–525

Strong C, Magnusdottir G (2011) Dependence of NAO variability on coupling with sea ice. Clim Dyn 36:1681–1689

Sun L, Deser C, Tomas RA (2015) Mechanisms of Stratospheric and Tropospheric Circulation Response to Projected Arctic Sea Ice Loss. J Clim 28:7824–7845

Thompson DW, Wallace JM (2000) Annular Modes in the Extratropical Circulation. Part I: Month-to-Month Variability. J Clim 13:1000–1016

Tomassini L, Gerber EP, Baldwin MP, Bunzel F, Giorgetta M (2012) The role of stratosphere-troposphere coupling in the occurrence of extreme winter cold spells over northern Europe. J Adv Model Earth Syst 4:M00A03. https://doi.org/10.1029/2012MS000177

Wang R, Tomkawa Y, Nakamura T, Huang K, Zhang S, Zhang Y, Yang H, Hu H (2016) A mechanism to explain the variations of tropopause and tropopause inversion layer in the Arctic region during a sudden stratospheric warming in 2009. J Geophys Res Atmos 121:932–945

Watson PAG, Gray LJ (2014) How does the quasi-biennial oscillation affect the stratospheric polar vortex? J Atmos Sci 71(1):391–409.

https://doi.org/10.1175/JAS-D-13-096.1

Waugh DW, Sobel AH, Polvani LM (2017) What is the Polar vortex and how does it influence weather? Bull Am Meteorol Soc 98:37–44. https://doi.org/10.1175/BAMS-D-15-00212.1

White I, Garfinkel CI, Gerber EP, Jucker M, Aquila V, Oman LD (2019) The Downward Influence of Sudden Stratospheric Warmings: Association with Tropospheric Precursor. J Clim 32(1):85–108. https://doi.org/10.1175/JCLI-D-18-0053.1

WMO (1957) Definition of the tropopause. WMO Bull 6:136

Wong S, Wang W-C (2003) Tropical-extratropical connection in interannual variation of the tropopause: Comparison between NCEP/NCAR reanalysis and an atmospheric general circulation model simulation. J Geophys Res 108(D2):4043. https://doi.org/10.1029/2001JD002016

Yang XY, Yuan X (2014) The Early Winter Sea Ice Variability under the Recent Arctic Climate Shift. J Clim 27:5092–5110

Yang XY, Yuan X, Ting M (2016) Dynamical Link between the Barents-Kara Sea Ice and the Arctic Oscillation. J Clim 29:5103–5122

Zängl G (2002) Dynamical heating in the polar lower stratosphere and its impact on the tropopause. J Geophys Res Atmos 107:4079. https://doi.org/10.1029/2001JD000662

Zängl G, Hoinka KP (2001) The Tropopause in the Polar Regions. J Clim 14:3117–3139

Zängl G, Wirth G (2002) Synoptic-scale variability of the polar and subpolar tropopause: Data analysis and idealized PV inversions. Q J R Meteorol Soc 128:2301–2315. https://doi.org/10.1256/qj.01.76

Zhang J, Tian W, Chipperfield MP, Xie F, Huang J (2016) Persistent shift of the Arctic polar vortex towards the Eurasian continent in recent decades. Nat Clim change 6:1094-1099

Zhang P, Wu W, Smith K (2018) Prolonged effect of the stratospheric pathway in linking Barents-Kara Sea sea ice variability to the midlatitude circulation in a simplified model. Clim Dyn 50:527–539.

https://doi.org/10.1007/s00382-017-3624-y

Zhang K, Wang T, Xu M, Zhang J (2019) Influence of Wintertime Polar Vortex Variation on the Climate over the North Pacific during Late Winter and Spring. Atmosphere 10(670):1–17. https://doi.org/10.3390/atmos10110670

국문 초록

북극 해빙 변화 및 북반구 대류권계면 변동성과 관련된 성층권-대류권 커플링의 계절내 진화 특성

김 진 주
지구환경과학부
서울대학교 대학원

북반구 겨울철의 성층권 극소용돌이 변동 및 관련 성층권-대류권 상호작용은 대류권 날씨의 계절내 예측에 있어서 중요한 요소들이다. 성층권-대류권 상호작용에 대해 좀 더 정확하게 이해하기 위하여, 본 연구에서는 해빙 및 대류권계면 변동과 관련해 성층권 극소용돌이 변동의 계절내 진화 특성을 면밀히 조사하였다.

먼저, 성층권 극소용돌이 변동에 영향을 미치는 요인 중 하나인 해빙 변동의 주요 모드가, 북극 온난화 증폭과 관련된 북극 해빙 감소 시그널과 북대서양 진동과 관련된 북대서양 쌍극 해빙 변동 시그널임을 확인하였다. 이는 바렌츠-카라해 해빙 감소의 가속화 시그널과 래브라도해 해빙의 십년규모 위상 감소 시그널을 반영하며, 두 해빙 변동 과정 모두 겨울철 성층권 소용돌이 약화를 동반한다. 하지만 해빙 변동 모드에 따라 성층권 극소용돌이 약화의 발생시기와 소용돌이의 위치 혹은 형태 변화는 다르게 나타났다. 첫번째 모드에서는 바렌츠-카라해의 해빙 감소와 함께 1월 중순에서 2월 말 동안에 소용돌이 약화가, 두 번째 모

드에서는 바렌츠-그린란드해 해빙 증가 및 래브라도해-허드슨만의 해빙 감소와 함께 12월에서 2월초까지 소용돌이 약화가 동반된다. 지역적 변동 관점에서는, 소용돌이 약화 편차가 가장 발달 했을 때에 성층권 소용돌이가 첫번째 모드에서 유라시아쪽으로 이동하고, 두 번째 모드에서 유럽쪽으로 국한되어 이동하는 경향이 있음을 확인하였다. 또한 두 개 해빙 모드의 다른 장주기 변동이 겨울철 성층권 극소용돌이 진화의 장기 평균 변화에 기여함을 확인하였다.

한편, 이런 특정 대류권 요인에 관련된 성층권 소용돌이 변동뿐만 아니라 성층권 소용돌이의 보편적인 계절내 진화 특성 또한 명확하게 이해되지 못하고 있다. 본 연구에서는 성층권과 대류권 사이의 경계면에 해당하는 대류권계면 변동의 주요 모드와 관련해 11월~4월 기간 동안의 성층권-대류권 연직 변동 특성에 대해 분석하였다. 결과는 주요 대류권계면 변동이 성층권 극소용돌이의 겨울철-이른 봄철 동안 지속되는 단일 위상 변동과 겨울철-봄철에 반대되는 2개 위상 변동의 직접적 영향을 받음을 확인하였다. 동서평균장 관점에서는 두 모드 모두에서 성층권 소용돌이와 대류권 고위도 순환장의 일관된 진화 양상이 특징적으로 나타났다. 하지만, 지역적 관점에서는 성층권 소용돌이와 대류권 제트 변동 사이에 비대칭적 관계가 존재함을 확인하였다. 특히 첫번째 모드에서는 2-3월에 성층권 극소용돌이 약화와 함께 대서양 제트축은 적도쪽으로 이동하지만 태평양 제트축은 극쪽으로 이동하는 경향이 있음이 확인되었다. 또한 성층권 극소용돌이 개별 이벤트들의 발달 구조 및 발달 시

기가 해마다 변동하는 것이 두 대류권계면 모드의 변동에 의존하고 있음을 확인하였다. 결과는 성층권-대류권 연직 변동의 주요 발달 특성 뿐만 아니라 개별 특성에 대한 심화된 이해를 가능하게 함으로써, 날씨의 계절내 예측성 향상에 도움을 줄 것으로 예상된다.

주요어: 성층권-대류권 커플링, 북극 해빙 변동성, 해빙-성층권 극소용돌이 관계, 대류권계면 변동성, 대류권계면-성층권 극소용돌이 관계

학 번: 2015-30983